2022-01-28

Flying Anemometers: Performance Assessment of a Miniaturized Sonic Anemometer for Measuring Wind from a Drone

Wearmouth, Clay

UNIVERSITY OF CALGARY

Flying Anemometers: Performance Assessment of a Miniaturized Sonic Anemometer for Measuring Wind from a Drone

by

Clay Wearmouth

A THESIS

SUBMITTED TO THE FACULTY OF GRADUATE STUDIES

IN PARTIAL FULFILMENT OF THE REQUIREMENTS FOR THE

DEGREE OF MASTER OF SCIENCE

GRADUATE PROGRAM IN GEOGRAPHY

CALGARY, ALBERTA

JANUARY, 2022

Abstract

This MSc thesis incorporates wind-tunnel testing and field trials to evaluate the performance of new miniaturized sonic anemometers for use onboard small aerial drones for meteorological measurements. Drones have received considerable attention as they provide a flexible vantage point for measuring in-situ atmospheric conditions. Specifically, drones equipped with miniaturized sonic anemometers may be suitable for measuring wind conditions in support of research and industrial emissions applications. These compact and lightweight anemometers are small enough to fit the restrictive payloads of small multirotor drones, however, mounting these sensors on a drone introduces several sources of error that have not been well documented. This noted, the objective of this MSc thesis is to evaluate the accuracy of wind measurements from a drone equipped with a miniaturized sonic anemometer. The research approach consisted of two stages. First, flight conditions and changes in pitch angle and yaw rotation were simulated from a fixed position in wind tunnel experiments to evaluate the anemometer's measurement accuracy in the absence of aerodynamic effects from platform motion and rotors. Next, a rotor wash analysis was performed to measure the airflow disturbance generated by the drone's rotors. These data were used to identify ideal locations for sensor placement where airflow is minimally disturbed. Results from wind tunnel testing indicate the anemometer systematically disturbs airflow when part of the sensor is upwind of the sampling volume. This interference impacts both wind speed and direction data. Results from the rotor wash testing revealed airflow is minimally impacted 50 cm above the rotors and wind direction is less affected over the upwind rotor pair. These relationships were investigated to optimally balance each factor to generate high quality in-situ atmospheric data from a miniaturized sonic anemometer mounted on a drone. Lastly, recommendations for flight tests are provided for future research. The outcome of this thesis research is a better-resolved understanding of wind measurement accuracy from drones using miniaturized sonic anemometers.

Acknowledgements

As this chapter of my academic career is ending, I find joy knowing I was surrounded by a large group of brilliant and generous people that truly made this a wonderful experience. I would like to thank my supervisor, Dr. Chris Hugenholtz, for providing unwavering support throughout this journey. I can't imagine where I would be without your guidance and occasional Dutch encouragement. Similarly, I would like to express my gratitude to my colleges in ES-922. Elena, thank you for being an inspiration and a role model. Adam, thank you for letting me bounce ideas off you for years, providing a helping hand when needed, and making sure the atmosphere in 922 remained cheerful regardless of any research-based frustrations. To the remaining mentors of 922: Thomas, Maja, Paul, Tyler, Mo, and Tom, your never-ending enthusiastic assistance made a world of difference that I will forever be grateful for. To Jack and Kale, I sincerely appreciate all the help you provided by actively assisting in my research and by being available for sports meditation. I would like to thank my family for creating an encouraging foundation that allowed me to grow into who I am today. A special thanks to my Mom for always being the first person to review my work. Thank you to Duff for offering to review this document while on vacation. Sir Admiral Beaufort, I appreciate your ability to create distractions and break up the monotony of working from home. Lastly, I would like to thank my partner Claire for providing the initial inspiration to start this program. You have been a continuing source of joy and motivation ever since I met you.

Table of Contents

List of Figures

List of Tables

List of Abbreviations, Symbols, and Nomenclature

ABL: Atmospheric Boundary Layer
AD: Anderson-Darling test for normality
CFD: Computational Fluid Dynamics
Cone of Acceptance: Maximum angles at which accurate measurements can be recorded
DJI: Dà-Jiāng Innovations
GNSS: Global Navigation Satellite System
Hz: Hertz
IMU: Inertial Measurement Unit
LCWT: Low-cost Wind Tunnel
MADE: Mean Absolute Direction Error
MAE: Mean Absolute Error
ME: Mean Error
DE: Mean Directional Error
MHPP: Multi-hole Pitot Probe
NFS: No Flow Sensor
RE: Relative Error
RPAS: Remotely Piloted Aircraft Systems/ Drone
RS – 232: Recommended Standard 232 communication
TSM: TriSonica-Mini
$\boldsymbol{I_u}$: turbulence intensity; a measure of random variations in wind speed and direction observations
UAV: Uninhabited Aerial Vehicle
α: alpha value/ Confidence Interval
Θ: pitch angle, or rotation around a horizontal axis
Ψ: rotation around a vertical axis

Chapter 1: Introduction

1.1. Motivation and Objectives

Remotely piloted aircraft systems (RPAS), also known as Uninhabited Aerial Vehicles (UAV) or drones are broadly used in a growing number of research and industrial applications involving atmospheric boundary layer (ABL) measurements (Elston et al., 2015; Suomi & Vihma, 2018). One of the technical challenges of using drones for atmospheric applications is the measurement of wind speed and direction from a moving airborne platform. Typical drones used for wind measurements in the ABL are small and have functional payload restrictions on the size and type of atmospheric sensors that can be mounted to the airframe. Conventional wind sensors are too bulky and heavy (Gill, 2019), which prompted recent developments in the design of lightweight, miniaturized wind sensors. However, there is very little published evidence to evaluate the performance of these sensors. As such, this MSc thesis research was initiated to fill this gap. The overall objective of this research was to evaluate the accuracy of wind speed measurements acquired by a miniaturized sonic anemometer mounted to a small multirotor drone. The following research questions were addressed:

1. What is the accuracy of wind measurements from a miniaturized sonic anemometer under different attitudes that reproduce conditions expected during flight?
2. How can the sensor's mounting location impact the wind measurements during flight?

The first research question was investigated by simulating the effects of a drone's attitude on wind measurement accuracy by angling the anemometer in configurations representing the attitude of the drone during different flight conditions. Whereas most anemometers are designed for static mounting configurations to measure wind speed, a drone's attitude changes according to the flight speed and wind conditions, which will change the angle of the anemometer. The goal is to document the error of the wind speed and direction estimates and determine if calibration can be applied to improve the measurement accuracy. The second research question evaluated how airflow inference

caused by a drone's rotors impact the measurements. The airflow above the drone was measured to determine regions of minimal interference. The goal was not to discriminate specific aerodynamic effects that impact observations, but rather to determine if strategic mounting positions improve the accuracy.

1.2. Literature Review

Modern drones have developed into powerful tools for a variety of research applications. A key feature of modern multirotor drones is the maneuverability of the aircraft. However, this can create a challenging aerodynamic environment for collecting accurate in-situ wind speed and direction measurements (Bartholmai & Neumann, 2010; Yeo et al., 2015; Alvarado et al., 2017; Hollenbeck et al., 2018; Prudden et al., 2018; Suomi & Vihma, 2018). Improving the accuracy of wind speed and direction estimation methods from drones has significant implications for their use in atmospheric research (Reuder et al., 2009; Martin et al., 2011; Schuyler & Guzman, 2017) and for improving flight control (Arain & Kendoul, 2014; Marino et al., 2015). This has been noted in recent emissions research (Nathan et al., 2015; Golston et al., 2018; Xing et al., 2019). As shown in Figure 1.1, the frequency of peer-reviewed publications with the keywords "UAV" and "wind sensor" have increased dramatically over the past 21 years.

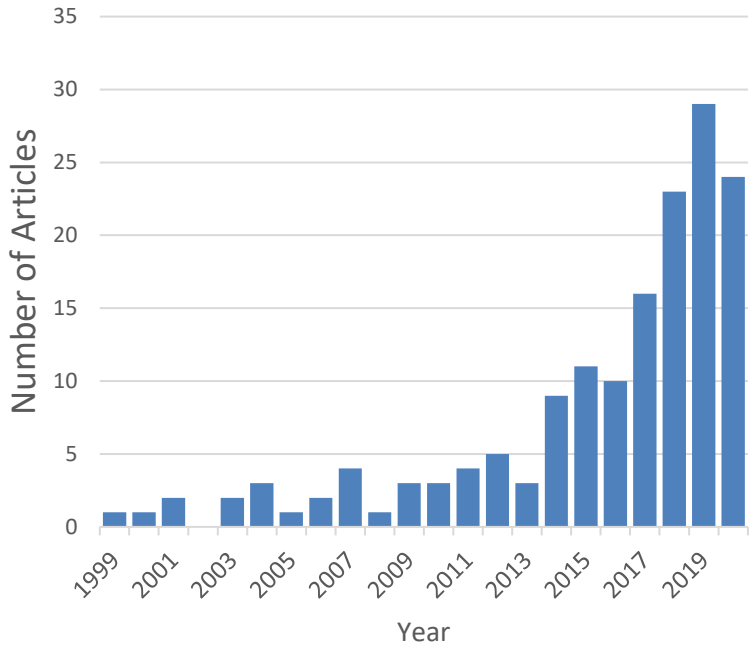

Figure 1.1: *Number of peer-reviewed publications with drones used for measuring wind. These data were derived from a basic search on Web of Science using the keywords "UAV" and "wind sensor".*

1.2.1. Drone Classes

Drone designs are generally categorized into two primary groups based on how the aircraft maintains flight: fixed-wing and rotary. Fixed-wing drones (Figure 1.2A) are similar to piloted airplanes. They typically have longer flight endurance; however, they have low maneuverability relative to rotary drones and require either large areas for take-off or launch assists such as a catapult or piston. Rotary drones such as helicopters or multi-rotors (Figure 1.2B) have the shortest flight endurance, but also have the ability to hover, take-off, and land vertically.

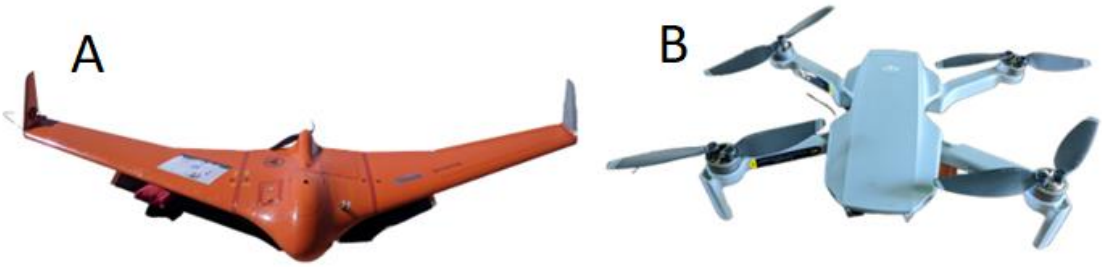

Figure 1.2: *Common drone designs.* **A)** *Fixed-wing Braemor.* **B)** *DJI Mavic Mini multi-rotor.*

Historically, fixed-wing drones have been the most common platform used in atmospheric research applications (Alvarado et al., 2017; Palomaki et al., 2017). Due to their long history of use and shared characteristics with piloted aircraft, fixed-wing drones have developed well-understood methods of estimating wind speed and direction (Konrad et al., 1970; Elston et al., 2015; Villa et al., 2016). However, the enhanced maneuverability of rotary drones makes developing robust methods of estimating wind speed and direction from the platform an attractive area of research.

1.2.2. Drone Based Wind Speed and Direction Estimation Methods

Wind speed and direction can be estimated from a drone using several different approaches that are broadly grouped into two categories based on how the wind measurements are obtained: direct and indirect. Direct methods include measurements from anemometers onboard the drone that measure the physical properties of air passing through a sampling volume. Examples of drone-mounted anemometers used for direct sampling include cup anemometers (Riddell, 2014), pitot tubes (Prudden et al., 2018), and sonic anemometers (Palomaki et al., 2017). Indirect methods sample data from instruments typically used for flight control to estimate wind speed and direction. Both approaches have unique properties that make specific methods more applicable to certain flight operations and drone classes. Generally, both methods require additional sensors such as a Global Navigation Satellite System (GNSS) and Inertial Measurement Unit (IMU) to derive the wind speed and direction. These components are now standard on most modern drones.

Drone-based wind speed and direction measurements are commonly evaluated for accuracy by comparing them to several types of reference data. Reference data can be collected using instruments mounted at or near the flight level on meteorological towers, remotely sensed (e.g., wind profilers), or extrapolated from the highest available measurement (van der Kroonenberg et al., 2008; Villa et al., 2016; Niedzielski et al., 2017; Rautenberg et al., 2018; Shimura et al., 2018; Suomi & Vihma, 2018; Hollenbeck et al., 2019).

1.2.3. Direct Methods of Estimating Wind Speed and Direction from a Drone

1.2.3.1. Pitot tubes

Fixed-wing drones are commonly equipped with pitot tubes to determine the platform's airspeed, similar to conventional piloted aircraft. Typically, pitot tubes have at least two openings with one or more forward-facing ports to measure the stagnation pressure, and one side opening to measure the static pressure. The difference between the stagnation and static pressures yields the dynamic pressure, which is related to the aircraft's airspeed (Klopfenstein, 1998). To calculate the wind vector from a pitot tube on a drone requires knowledge of two other vectors: the flight vector and the ground vector of the aircraft (Mayer et al., 2012; Rautenberg et al., 2018). This combination of vectors is known as the wind triangle (Wang et al., 2018; Figure 1.3). The flight vector is the airspeed collected by the pitot tube, while the ground vector is determined using onboard GNSS. The air vector and ground vector can be substituted into the wind triangle equation to determine the true wind speed. The difference between the ground and air vector is the influence of the wind.

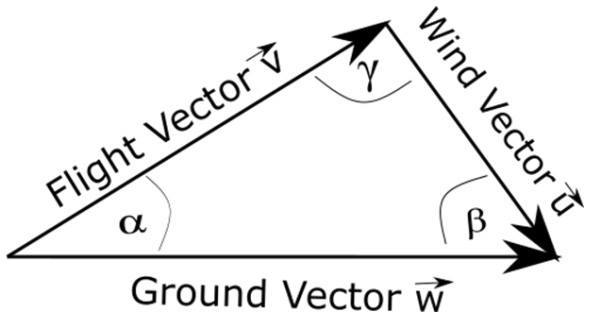

Figure 1.3: *Diagram of the wind triangle vector components (adapted from Neumann et al. (2010)).*

Pitot tubes are known to suffer from several sources of error on drones. First, they are unidirectional sensors that require the stagnant port or sensor tip to be pointed within a cone of acceptance in relation to the mean airflow (Shepherd, 1981; Figure 1.4). The wind speed estimate is unreliable if the direction of the mean airflow is outside the cone of acceptance. Small perpendicular wind vectors can cause the mean wind direction to exceed the cone of acceptance (Rautenberg et al., 2018). The cone of acceptance can be increased by using a type of pitot tube called a multi-hole pitot probe (MHPP), which uses several stagnant ports angled at different directions to overcome some of the directional limitations encountered by a standard Pitot tube (Shepherd, 1981; Elston et al., 2015).

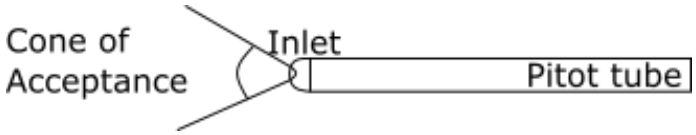

Figure 1.4: *Diagram of a Pitot tube and an example of the cone of acceptance. If the mean wind direction is outside the cone of acceptance the observational accuracy will decrease.*

Generally, pitot tubes are mounted on the nose of fixed-wing drones or extended in front of the platform on multi-rotors. Drones with integrated pitot tubes can estimate wind speed and direction with accuracies better than ±1 ms^{-1} and less than 10° when compared to a reference measurement (van der Kroonenberg et al., 2008; Cho et al., 2011; Niedzielski et al., 2017; Rautenberg et al., 2018). However, due to the unidirectional limitations of pitot tubes, a significant underestimation of

horizontal wind speed has been noted during periods of turbulent airflow and steep ascents or descents (Reineman et al., 2013; Niedzielski et al., 2017; Rautenberg et al., 2018).

MHPPs overcome some of the unidirectional limitations encountered by pitot tubes and can provide accurate horizontal and vertical wind speeds during mild turbulence (Prudden et al., 2018). However, MHPPs still encounter measurement limitations during quick maneuvers or steep ascents and descents (Reineman et al., 2013). Drones equipped with MHPPs have provided horizontal and vertical wind speed and direction observations accurate to within 1 m s^{-1} and 5° of ground-based or met-tower reference instruments (van der Kroonenberg et al., 2008; Prudden et al., 2017). Other authors have recorded wind speed errors of less than 3 cm s^{-1} using MHPP during ground tests but were unable to verify these values during flight tests (Reineman et al., 2013).

1.3.3.2. Inertial Anemometers

Inertial anemometers calculate wind speed by measuring how fast airflow rotates a propeller, impeller, or a set of cups around a vertical or horizontal axis. The angular velocity of rotation is proportional to the wind speed. Cup anemometers are robust sensors commonly found on meteorological towers where they are used for long-term observations. Standard cup anemometers cannot be used to determine wind direction, so the sensor is often paired with directional sensors such as wind vanes. Modern cup anemometers can achieve accuracies of ±1% up to wind speeds of 60 m s^{-1} (Sotelino et al., 2012). However, due to the inertia stored in the rotating cups, cup anemometers are prone to over-speeding as the cups will continue to spin even after the wind speed has reduced (Wyngaard, 1981). Over-speeding may also occur in turbulent airflow where a substantial vertical wind component is present (Kristensen, 1998; Giebel et al., 2012). Additionally, cup anemometers may under-speed at very low wind speed (< 1 m s^{-1}) due to internal friction between bearings (Kristensen, 1999).

Inertial anemometers are rarely used on mobile measurement platforms due to their sensitivity to turbulence and vertical wind (Kristensen, 1998). The large profile of cup anemometers can be a challenge for use on fixed-wing drones as the sensor would need to be mounted in a location where it can record unimpeded wind and not interfere with flight dynamics (Giebel et al., 2012; Hollenbeck et al., 2018). However, the use of cup anemometers has been tested on rotary drones (Riddell, 2014). In that research, the cup anemometer was mounted on a boom in front of the aircraft to reduce the influence of the rotor wash on the sensor. Riddell (2014) found that the airborne cup anemometer consistently overestimated the wind speed when compared to a reference instrument but demonstrated the potential of this method.

1.3.3.3. Sonic Anemometers

Sonic anemometers are non-mechanical sensors (i.e. no moving parts) that determine the wind speed and direction by monitoring repetitive sonic pulses between pairs of transducers. These pulses travel between the transducer pairs at the speed of sound and can be influenced by the wind passing through the sampling volume. The wind can increase or decrease the time it takes for a sonic pulse to reach the opposing transducer. This deviation can be attributed to the wind adding or subtracting energy from the pulse. Additionally, by combining more than one pair of transducers on different axes, the wind direction can be calculated from the same process. The anemometer needs to be calibrated to the ambient environmental conditions as changes in humidity, pressure, and temperature can change the speed of sound through the air.

Because sonic anemometers have no moving parts, they are not prone to inertial issues that are encountered by cup anemometers. Until recently, sonic anemometers have been too large and fragile for drone applications. But new miniaturized models such as the TriSonica-Mini (TSM) and Decagon Devices DS-2 have been developed as drone-capable sensors. Miniaturized sonic anemometers have been installed on both fixed-wing and multirotor drones (Palomaki et al., 2017; Hollenbeck et al.,

2018; Shimura et al., 2018). Similar to the other methods, drones using sonic anemometers also require onboard GNSS to extract the wind vector from the wind triangle and an IMU to resolve potential state estimate errors.

Several types of sonic anemometer designs are found in research-grade instruments. Typically, 2D sonic anemometers feature two transducer pair, whereas 3D sonic anemometers generally have three transducer pairs. 3D sonic anemometers can be split into two categories: orthogonal and non-orthogonal. Generally, orthogonal sonic anemometers have four transducer pairs offset by 90°, and non-orthogonal sonic anemometers have three transducer pairs offset by 120° (Suomi & Vihma, 2018). These transducer configurations create different aerodynamic disturbances that can impact the airflow before it can be measured (Diego & Jolla, 2016). Some new miniaturized designs differ from the typical 3D sonic anemometer transducer layout as they only feature two pairs of orthogonal transducers, which may create aerodynamic disturbances unique to this design.

Sonic anemometers are known to suffer from several sources of error that can influence the accuracy of wind measurements, including steep angles of attack errors (Wilczak et al., 2001; Gash & Dolman, 2003; Nakai et al., 2006; Nakai & Shimoyama, 2012) and transducer shadowing errors (Wyngaard & Zhang, 1985; Kaimal et al., 1990; Wieser et al., 2001; Frank et al., 2015). Errors from steep angles of attack occur when an anemometer begins to interpret horizontal wind as vertical wind and vice-versa (Wilczak et al., 2001; Hollenbeck et al., 2019). This can be caused by mounting the anemometer in a non-level position, or when the mean wind direction is not parallel to the sensor. The angle at which a sonic anemometer begins to encounter errors caused by steep angles of attack varies with each model but can cause significant cross-contamination between the vertical and horizontal wind components. In the context of aircraft-mounted sonic anemometers, an onboard IMU can be used to record the aircraft's attitude throughout the flight so that angle of attack errors can be identified.

Transducer shadowing errors occur when the anemometer support structures or transducers distort the airflow before the sensor can measure the true wind speed and direction (Wieser et al., 2001; Frank et al., 2015; Huq et al., 2017). Additionally, turbulent airflow created by the drone's body and rotor wash may interfere with the anemometer if the sensor is not mounted in an appropriate location (Hollenbeck et al., 2018). The interference caused by these factors is also known to change based on the orientation of the drone relative to the wind direction and with airspeed (Smith et al., 2016). Figure 1.5 shows a computer simulation of transducer shadowing effects, wherein the anemometer's front support strut partially blocks airflow before the sensor can measure the true wind speed. The dark blue and light blue areas within the sensor sampling area indicate the airflow is slowed due to interference caused by the upwind vertical strut. The simulation in Figure 1.5B illustrates how the front vertical strut and transducer can impact the instantaneous wind direction.

The impact of transducer shadowing and steep angles of attack on the observational accuracy of sonic anemometers is well known. Thus, several common methods of error quantification are used. The most common method uses a controlled aerodynamic environment or wind tunnel to iteratively determine the relative error in different orientations and wind speeds. These methods compare the samples recorded by the sonic anemometer against a reference instrument to determine the observational error. Another method to evaluate the observational error uses several sonic anemometers of the same manufacturer and model positioned in different orientations to compare the different results against each other (Nakai & Shimoyama, 2012). Wind speed and direction error are often presented as the residual difference between the sonic anemometer and reference (Van Der Molen et al., 2004). Similarly, wind speed error is also presented as the residual difference relative to the ambient wind speed (Grelle & Lindroth, 1994; Högström & Smedman, 2004). Both metrics provide valuable insight in different situations. The residual method is useful for demonstrating the magnitude of error, while the other metric shows the severity of the errors relative to the ambient wind

speed. In both methods, wind speed and direction errors are commonly reported as the mean error for a specific duration of time (Peña et al., 2019).

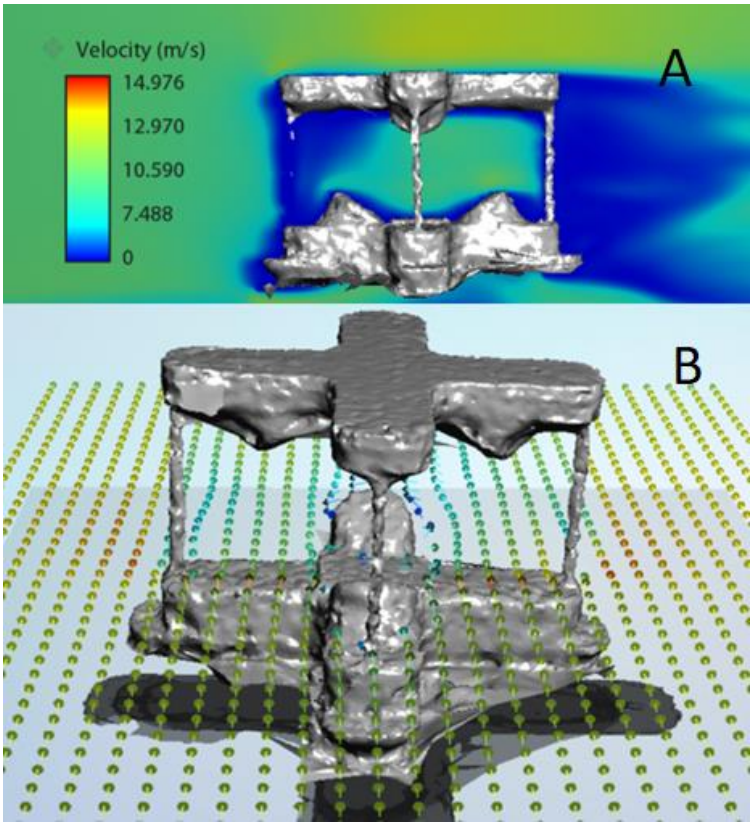

Figure 1.5: A) *Computational fluid dynamics (CFD) simulation of transducer shadowing from support struts on a sonic anemometer. Regions that are blocked and slowed down are identified as the dark and light blue regions.* **B)** *CFD simulation of transducer shadowing causing a change in the instantaneous wind direction.*

Errors caused by steep angles of attack and transducer shadowing are well-known challenges. New developments in anemometry have created an opportunity for sonic anemometers to be mounted on small consumer-grade drones. However, the complex aerodynamics that surrounds an unstable drone is a new and challenging context for sonic anemometer operation. Most of the literature surrounding common errors encountered by sonic anemometers has focused on sensors fixed to

stationary masts where changes in the wind regime happens gradually. Compared to anemometers mounted on stationary objects (e.g., towers), ones mounted to drones will encounter rapidly changing wind directions, wind speeds, and flight attitudes, which can all attribute to errors in the measured wind speed and direction. Small modern drones can reach angles of attack greater than the maximum pitch angle at which some sonic anemometers can reliably observe the wind speed and direction. Thus, the impact of drone flight dynamics, specifically steep angles of attack have on sonic anemometer's wind speed and direction observations is relatively unknown.

Early attempts using a sonic anemometer to resolve wind speed and direction from rotary drones were challenged by anemometer and aircraft design limitations. Giebel et al. (2012) attached an RM-Young 81000 3D sonic anemometer to a helicopter drone as a slung load 5 meters below the aircraft. The tests showed that it was feasible to use a 3D anemometer to collect wind speed and direction from drones, but also highlighted a number of challenges and limitations. More recent tests using miniaturized 2D sonic anemometers on multirotor drones have been able to resolve wind speed and direction during hovering and flight tests to within ±0.6 m s^{-1} and ±12° (Shimura et al., 2018) to ±30° (Palomaki et al., 2017) of a reference instrument. However, both studies chose to not address errors relating to steep angles of attack and transducer shadowing. Palomaki et al. (2017) noted that miniaturized 3D sonic anemometers could mitigate the impact of errors caused by the angle of attack during flight. These studies mounted the sonic anemometer 30 cm (Palomaki et al., 2017) and 39 cm (Shimura et al., 2018) above the rotor plane, which was likely not high enough to be free of turbulent flow caused by rotor wash (Hollenbeck et al., 2018).

Ideally, a sonic anemometer is mounted in a location where it does not impede the flight dynamics of the drone and the sensor accuracy is not impacted by the rotor wash interference. The aerodynamic profile of rotor wash disturbance differs for each model of drone so prior testing is required for each design. A common method of measuring turbulence around a drone is to mount the

aircraft on a mast in an aerodynamically stable or controlled environment such as a wind tunnel. Next, the aircraft is instructed to hover while wind speed measurements are taken above the rotors. Results from rotor wash tests show that airflow is not significantly disturbed by rotor wash around 40-45 cm above the center of the drone (Alvarado et al., 2017; Hollenbeck et al., 2018). The impact of rotor wash is variable depending on several parameters including aircraft attitude, rotor RPM, wind speed, and wind direction. Interestingly, higher wind speed can reduce the impact of rotor wash as these external winds can push or shift the disturbed air away from the sensor (Hollenbeck et al., 2018). Before a sonic anemometer is mounted on a drone, the aerodynamic disturbances created by the rotors should be examined to minimize and quantify any potential error.

Fixed-wing drones encounter similar aerodynamic challenges when using sonic anemometers. Sensor placement on a fixed-wing drone needs to ensure that flight dynamics are not impeded while also avoiding areas of turbulent airflow. One location that has been identified as meeting the requirements is under the wing next to the fuselage. However, this location is blocked from effectively measuring perpendicular winds and can encounter significant noise caused by wing vibration (Hollenbeck et al., 2018). More work is needed to determine if miniaturized sonic anemometers can be used on fixed-wing drones.

1.3.4. Indirect Wind Speed and Direction Estimation Approaches

Not all drones can accommodate anemometers due to their size and carrying capacity, or because the additional components change their flight control and performance of the aircraft. An alternative approach is to estimate wind speed and direction indirectly from the state variables of the drone. Manufacturers such as Dajing Innovations (DJI) include wind speed and direction algorithms in the flight control software to warn pilots of dangerously high-air speeds. The least complex variants of the state variable approach only require ground speed data collected from an on-board GNSS (Mayer et al., 2012), while other more complex methods require additional aircraft parameters from several

flight instruments, and prior aerodynamic tests (Marino et al., 2015). State variable approaches rely on a relationship between aircraft attitude, drag, and ground speed to determine wind speed (Neumann & Bartholmai, 2015). State variable approaches follow a similar procedure to those methods that use the wind triangle to determine the true wind speed. However, the methods used to determine the vector components of the wind triangle differ between state variable approaches.

The least complex method of determining wind speed and direction applies to fixed-wing drones flying with a constant throttle and at an assumed constant airspeed. In the approach known as the "no-flow-sensor" (NFS), groundspeed is dependent on the angle between the drone's heading and wind direction (Mayer et al., 2012). The NFS method typically requires repeated flight circuits so the aircraft encounters headwind, tailwind, and perpendicular wind transects. Any deviation between the ground speed and the assumed constant airspeed is the result of additional forces caused by wind. The vector sum of the airspeed and groundspeed can be substituted into the wind triangle to determine wind speed.

In optimal conditions, the NFS can estimate an average wind speed for a full flight circuit to less than ±1.24 m s^{-1} when compared to an average collected from a reference instrument (Bonin et al., 2013; Rautenberg et al., 2018) and in simulated trials (Mayer et al., 2012). However, several operational limitations of this method reduce the certainty of the NFS. The NFS requires a consistent flight plan for the best results as this method is sensitive to turbulence and rapid maneuvers (Rautenberg et al., 2018). Additionally, the NFS is sensitive to non-horizontal flight paths resulting in a limited ability to collect data while climbing or descending (Mayer et al., 2012; Rautenberg et al., 2018). Further, in unstable conditions or averaging periods less than a half loop, NFS can only resolve wind speed to less than ±3 m s^{-1} compared to a reference instrument (Rautenberg et al., 2018). Several variations of state variable approaches are being developed that overcome the limited resolution of the NFS by integrating additional flight control sensors into the wind estimation procedure. Inertial

methods expand upon the NFS method and have been used to determine wind speed and direction from multirotor drones with more frequent observations.

Multirotor drones maintain flight by balancing a relationship between the force of gravity, drag, lift, and thrust. To move in a horizontal direction the multirotor tilts to create an imbalance between the force of thrust and drag. As the tilt angle increases a larger imbalance between thrust and drag is created resulting in more horizontal speed. The tilt angle also changes to compensate for increased drag caused by variations in wind speed. An example free body diagram of the force components of a multirotor drone in flight is shown in Figure 1.6. As the drone pitches forward to overcome the additional horizontal drag caused by a headwind the vertical thrust is transferred to horizontal thrust. The pitch angle required to transfer enough vertical thrust to horizontal is proportional to the wind speed. If the relationship between airspeed and tilt is understood, the multirotor tilt can be used to estimate the flight vector (Neumann & Bartholmai, 2015; González-Rocha et al., 2019). The relationship between tilt and airspeed is determined by the drone's coefficient of drag. A higher coefficient of drag results in a larger drag force and therefore a steeper angle of attack is required to balance thrust and drag. Preliminary testing is required to determine the relationship and can be completed in a wind tunnel (Neumann & Bartholmai, 2015) or in calm conditions outdoors (Brosy et al., 2017). This relationship has been used to determine wind speed and direction from hovering and mobile observations. The airspeed collected through the IMU and reference data can be substituted into the wind triangle along with ground speed data from a GNSS to determine the wind speed. For example, if prior testing shows that a drone flying at 5 m s^{-1} should be tilted 6° forward, but the drone is tilted to 9°, the additional tilt is caused by increased drag induced by the headwind.

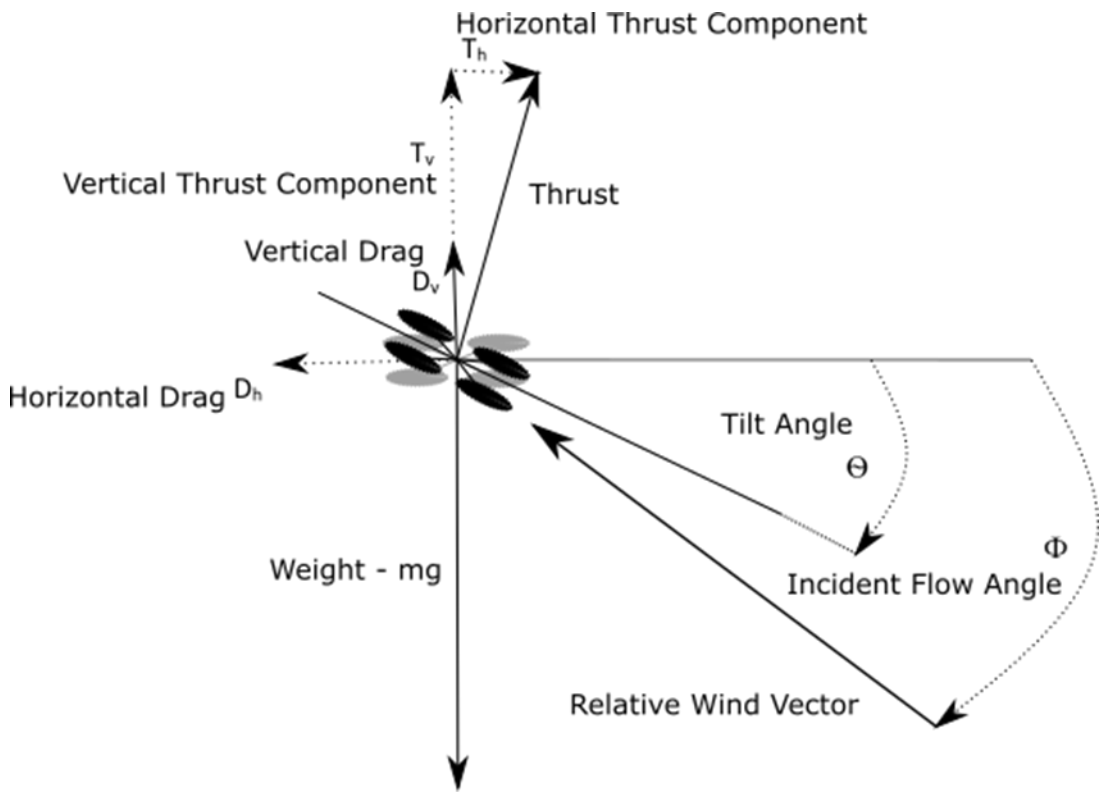

Figure 1.6: *Free body diagram of multi-rotor force components (adapted from Marino et al., 2015). The diagram illustrates the relationship between several vector components. Increased tilt angle is required to overcome the additional horizontal drag caused by increased head wind speed. Vertical thrust is then transferred to horizontal thrust to balance each force.*

Alternatively, the relationship between thrust and drag can be used to determine wind speed and direction by comparing the thrust differential between each motor of a multirotor drone (Marino et al., 2015; Hüllmann et al., 2018). Similar to the inertial method, differential thrust methods determine the relationship between how much thrust is required to overcome drag caused by variations in wind speed. For example, a multi-rotor drone flying into a headwind requires a higher energy output from the rear rotors than the front rotors. Thrust differential can be measured using the power draw from each motor (Marino et al., 2015) or phototransistors monitoring rotor RPM (Hüllmann et al., 2018). If the relationship between rotor output and airspeed is known, the result can be inserted into the wind triangle to determine wind speed.

Thrust differential methods have shown to be limited in their practicality. It was noted that the phototransistor method could only be used in low light settings and the rotors rotate so quickly the results were significantly noisy (Hüllmann et al., 2018). The power draw method also encountered limitations as rotary drones can produce vortex ring states where turbulence below the rotors can result in unpredictable thrust (Marino et al., 2015) and the power supply from the drone's battery cannot output consistent voltage throughout a flight (Hüllmann et al., 2018).

1.4. Summary

Fixed-wing drones have a long history as atmospheric research tools with well-established methods of measuring wind from the platform (Konrad et al., 1970; Rautenberg et al., 2018). However, the limited maneuverability of fixed-wing drones means they are not able to safely operate close to the ground or near infrastructure. These factors limit their effectiveness for many applications. Multirotor drones overcome these limitations with improved maneuverability but encounter challenging aerodynamics that can interfere with sensor performance (Smith et al., 2016).

Newly-developed miniaturized sonic anemometers have the potential to be installed on multirotor drones and provide local wind speed and direction. However, some of the testing approaches used to date do not fully address sources of error caused by the platform's attitude and aerodynamics (Palomaki et al., 2017; Prudden et al., 2018; Shimura et al., 2018). Understanding how these sources of error impact the reliability of the measurements will help determine if or how multirotor-drone-mounted sonic anemometers can be used for measuring wind speed and direction effectively (Hollenbeck et al., 2018, 2019). These sources of error need to be examined in detail to improve the technology and the reliability of measurements for research and industrial applications.

Chapter 2: Methodology

2.1. Overview

This thesis research evaluated the performance of the TriSonica Mini (TSM) 3D sonic anemometer (Figure 2.1). The TSM is a newly released miniaturized sonic anemometer developed by Anemoment, LLC. The manufacturer advertises the TSM as a drone-mountable sensor. The current model of TSM is 9.1 cm × 9.1 cm × 5.2 cm and weighs 50 g. With the current firmware release (v.1.74), the TSM is capable of measuring 3D wind up to an angle of attack of ±15° (Anemoment, 2019). The TSM has four orthogonal measurement paths and internally determines the path with the most distortion and removes it from the wind calculations. The TSM is symmetrical along its north and east axes. The north and east axes are also referred to as the U and V axes, respectively. Each of the struts is labeled with a cardinal direction in Figure 2.1. The TSM has a transducer pair on the upper portion of the sensor along the North-South axis and second pair on the base of the sensor along the East-West axis. Wind direction observations are relative to the front of the sensor. If the airflow is traveling from the north strut to the south strut the wind direction is recorded as 0°. Similarly, if the airflow was traveling from the east strut to the west the wind direction is 90°.

The TSM has a low energy consumption and can be powered by an external battery via a USB connection. The sensor specifications are summarized in Table 2.1. The TSM can estimate wind speed up to a maximum of 50 m s^{-1}, outputting digital data as a text file at a user-determined rate of 1, 2, 5, or 10 Hz. The TSM features a unique transducer layout with two transducer pairs. Data collected by the TSM used in this research is output via RS-232 or USB as a text file. For this assessment, the parameters that were used are wind speed, wind direction, horizontal wind speed, perpendicular wind speed, vertical wind speed, temperature, humidity, pressure, pitch, roll, and, heading.

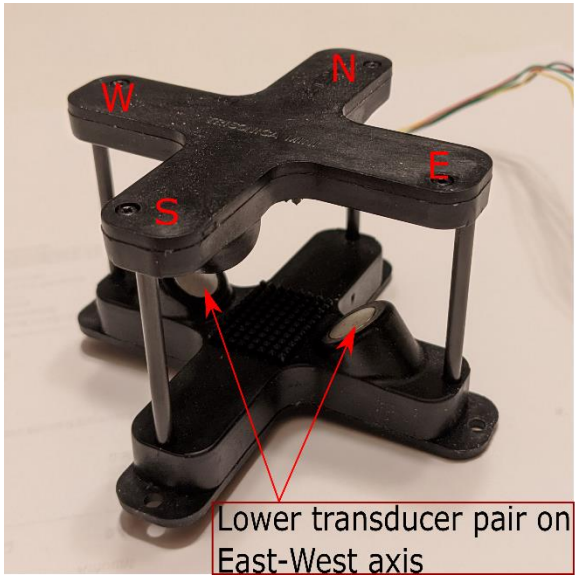

Figure 2.1: *The TriSonica Mini 3D sonic anemometer. Each strut and transducer has been labeled with a cardinal direction for identification.*

Table 2.1: *Overview of TriSonica-Mini Specifications (Anemoment, 2019).*

Sensor Specifications		**Wind Speed**	
Size	9.1 cm x 9.1 cm x 5.2 cm	Range	0 - 50 m s^{-1}
Weight	50 grams	Resolution	0.1 m s^{-1}
Power	9-36 VDC @ 30mA	Accuracy (0-10 m s^{-1})	±0.1 m s^{-1}
Digital Output Rate	1 Hz, 2 Hz, 5 Hz, 10 Hz	Accuracy (11-30 m s^{-1})	±1.0%
Operating Frequency	60 kHz	Accuracy (31 - 50 m s^{-1})	2.00%
Wind Direction		**Temperature**	
Range (x/y)	0-360°	Range	-40° C to +80° C
Range (z)	±30°	Resolution	0.1° C
Resolution	1.0°	Accuracy	±2°
Accuracy	±1.0°		
Humidity		**Pressure**	
Relative Humidity (0-100%)	±5%	Pressure (50-115 kPa)	±1 kPa
Tilt		**Compass**	
Pitch and Roll	±1.0°	Magnetic Heading	±5°

The methodology is structured into two parts. The first section examines the anemometer performance in a static position under different angles of attack in wind tunnel experiments. This simulates the angles expected during drone flight and establishes the anemometer angle as an independent variable. The goal is to isolate the wind speed and direction error, and to derive correction factors for different angles. The second component tests the rotor wash generated by the M100 while in a simulated hover. The goal for the rotor wash test was to identify ideal areas for sensor placement above the M100 where the airflow is minimally disturbed by rotor wash.

2.2. Indoor Testing: Angle of Attack & Transducer Shadowing Assessment

A series of wind tunnel experiments were conducted to assess the effect of attack angle on the accuracy of wind speed and direction recorded by the TSM. The assessment followed an iterative approach similar to Van Der Molen et al. (2004) and Nakai et al. (2012). Each iteration evaluated different combinations of pitch angle, yaw rotation, and wind speeds to create an overall measurement accuracy.

The wind tunnel used in these series of experiments is housed at the University of Calgary (Figure 2.2). This is a blowing-type wind tunnel that can generate laminar wind speeds ranging from 3-18 m s^{-1}. The outlet of the tunnel is equipped with an Ashcroft model CXLdp pitot tube that serves as the reference wind speed measurement for the experiments. The pitot tube has a wind speed accuracy of 0.4% (Ashcroft, 2009). The wind tunnel itself can be used as a reference for wind direction. Because the true wind direction is consistent with the orientation of the wind tunnel, the accuracy of the TSM can be assessed as the difference between the tunnel orientation and the TSM wind direction estimate. The Ashcroft pitot tube was set to record data at a rate of 5000 Hz, however, the observation frequency was reduced during the analysis to match the TSM recording frequency of 10 Hz.

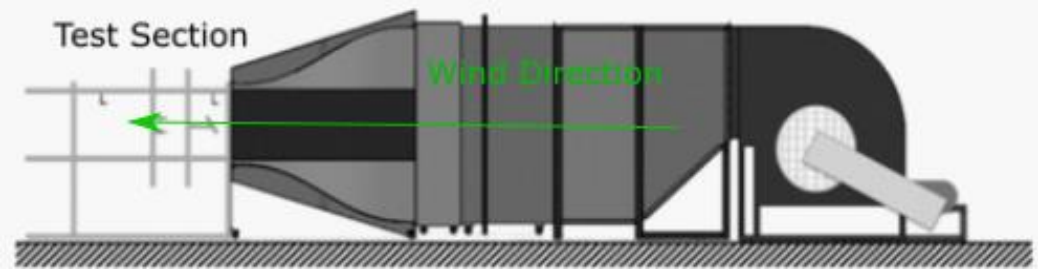

Figure 2.2: *Diagram of the blowing-type wind tunnel. The test section and direction of flow are indicated in the image (retrieved from https://schulich.ucalgary.ca/ltrac/facilities).*

Test runs progressed through different combinations of pitch, yaw, and wind speeds to evaluate the accuracy of the TSM in simulated drone flight angles (Figure 2.3). Each run evaluated one unique configuration at a constant wind speed and lasted 1 minute (or 600 samples). The yaw and pitch angles were measured using an XSens MTi-G-710 inertial measurement unit (IMU) for each test. The first configurations aligned the wind tunnel with the TSM so the sensor's front or North-South transducer pair were parallel to the airflow ($\psi = 0°$). Each test iteration increased the yaw angle counterclockwise by 10° up to 90°. At 90° of rotation, the East-West transducer pair were parallel with the wind tunnel. After 10 iterations, the yaw angle was reset to 0° and the pitch angle was increased or decreased by 10°. This procedure was repeated for pitch angles of 0°, 10°, 20°, 30°, -10°, -20°, and, -30°. The combinations of yaw rotation and pitch angle that were tested are displayed in Table 2.2. The 20° and 30° pitch angles are above the maximum angle of attack of the TSM specifications, but are attainable attitudes for modern multirotor drones. Following the completion of a set of runs, the wind speed inside the tunnel was increased and the process was repeated. Testing for each configuration started with the wind speed set to 3 m s^{-1}, then repeated at 10 m s^{-1}, and 14 m s^{-1}. These wind speeds were selected as they test two of the TSM accuracy ranges (Table 2.1) and are near the maximum wind speed tolerance of the DJI M100 drone used in the rotor wash testing (§ 2.3). A total of 70 test runs were completed at each test wind speed. Because the TSM is symmetrical along

the X- and Y-axis, anemometer roll can be excluded inside the wind tunnel (Hollenbeck et al., 2018). For example, a roll angle of -10° is the same as a -10° pitch and a 90° yaw rotation.

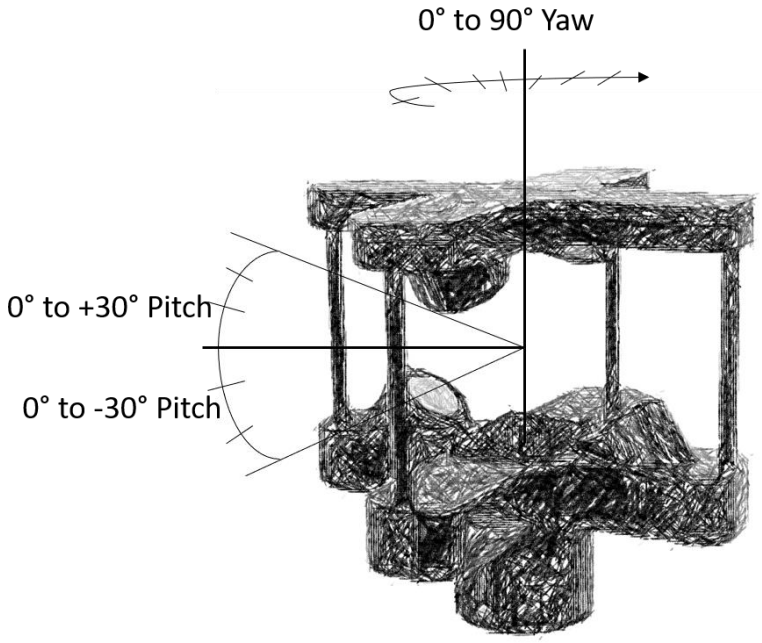

Figure 2.3: *Example diagram of test angles. Each tick mark is separated by 10° and represents a test angle. Each combination of pitch angle and yaw rotation is completed once during each test speed.*

Table 2.2: *Wind tunnel testing: pitch angle and yaw rotation procedure. This process was repeated three times, once at each tested wind speed.*

Test Number	Yaw (ψ)	Pitch (θ)	**Test Number**	Yaw (ψ)	Pitch (θ)	**Test Number**	Yaw (ψ)	Pitch (θ)
1	0	0	**26**	50	20	**51**	0	-20
2	10	0	**27**	60	20	**52**	10	-20
3	20	0	**28**	70	20	**53**	20	-20
4	30	0	**29**	80	20	**54**	30	-20
5	40	0	**30**	90	20	**55**	40	-20
6	50	0	**31**	0	30	**56**	50	-20
7	60	0	**32**	10	30	**57**	60	-20
8	70	0	**33**	20	30	**58**	70	-20
9	80	0	**34**	30	30	**59**	80	-20
10	90	0	**35**	40	30	**60**	90	-20
11	0	10	**36**	50	30	**61**	0	-30
12	10	10	**37**	60	30	**62**	10	-30
13	20	10	**38**	70	30	**63**	20	-30
14	30	10	**39**	80	30	**64**	30	-30
15	40	10	**40**	90	30	**65**	40	-30
16	50	10	**41**	0	-10	**66**	50	-30
17	60	10	**42**	10	-10	**67**	60	-30
18	70	10	**43**	20	-10	**68**	70	-30
19	80	10	**44**	30	-10	**69**	80	-30
20	90	10	**45**	40	-10	**70**	90	-30
21	0	20	**46**	50	-10			
22	10	20	**47**	60	-10			
23	20	20	**48**	70	-10			
24	30	20	**49**	80	-10			
25	40	20	**50**	90	-10			

The test procedure was developed to resolve the effects of different attack angles on the TSM wind speed and direction measurement accuracy. As part of the experiment procedure, the TSM was calibrated according to the manufacturer's specifications (Anemoment, 2019). The sensor was fastened to a ball and socket mount on a support beam in the center of the wind tunnel test section near the reference pitot tube (Figure 2.4). This mount allows for subtle variations in the attack angle and

yaw of the TSM. Angles were measured with the XSens IMU. The XSens can measure pitch to ±0.3° and yaw to ±0.8°. The TSM and pitot tube data were time-synchronized to within a second by manually triggering recording software at the same time.

Figure 2.4: *TriSonica Mini angle of attack test set up. The Pitot tube used as the reference instrument is the slender tube with a 90° bend above the TriSonica Mini.*

The observational accuracy of the TSM was calculated using two metrics. The first metric used by Van Der Molen et al. (2004), calculates the difference between the mean pitot tube observation and mean TSM observation. This metric was chosen because it provides valuable information on the magnitude of errors. Additionally, using the mean of each instrument limits the

impact of sudden changes in the room conditions. For example, a door opening into the room causes a noticeable change in pressure. The mean error (ME) was calculated as:

$$\boldsymbol{ME} = \frac{\mathbf{1}}{\boldsymbol{N}}\sum_{\boldsymbol{i=1}}^{\boldsymbol{N}}\left(\boldsymbol{u_{pitot}} - \boldsymbol{u_{TSM}}\right) \quad (1)$$

where *ME* is the mean difference between the pitot tube and the TSM wind speed observations.

The mean absolute error (MAE) is used to show how far a series of TSM observations are from the reference regardless of over and underestimations. The MAE is calculated as:

$$\boldsymbol{MAE} = \frac{1}{N}\sum_{i=1}^{N} |\, u_{pitot} - u_{TSM}| \quad (2)$$

u_{pitot} and u_{TSM} are defined as:

$$u_{pitot} = \frac{\sum_{i=1}^{n} x_i}{n} \qquad u_{TSM} = \frac{\sum_{i=1}^{n} x_i}{n} \quad (4)(5)$$

where x is the ith sample.

The second metric calculates accuracy relative to the wind speed as the ratio of the mean TSM observation divided by the mean wind speed recorded by the pitot tube (Grelle & Lindroth, 1994; Högström & Smedman, 2004; Diego & Jolla, 2016). This metric was chosen to show the error relative to the ambient wind speed. The relative error (RE) is calculated as:

$$RE = \frac{u_{TSM}}{u_{pitot}} \quad (6)$$

The TSM's wind direction observations were evaluated using a procedure similar to the wind speed assessment. However, instead of using a reference instrument to indicate the wind direction, the orientation of the wind tunnel was used. The direction of airflow inside the tunnel is consistent with the bounding walls of the structure. Therefore, the tunnel structure can be used as a reference for wind direction. As mentioned during the wind speed assessment, the TSM's orientation was measured using the XSens IMU. After the TSM orientation was adjusted and verified by the IMU, the orientation of the wind tunnel was recorded as the wind direction reference. This was accomplished by placing the IMU in the corner of the testing area. The IMU was placed in the corner against the vertical and horizontal beams to ensure all measurements were consistent.

Wind direction observations from the TSM are relative to the front transducer, meaning airflow parallel to the front or North transducer was registered as a wind direction of 0°. As the TSM was rotated, the wind direction estimate should match the amount of yaw rotation applied for each test orientation. Similar to Wieser et al. (2001) and Diego et al. (2016), the mean directional error (DE) was calculated as the mean difference between the wind tunnel azimuth or reference direction and TSM wind direction estimate. Figure 2.5 is an example of how wind direction observations were assessed. Samples with a wind direction greater than the test's yaw rotation represent overestimations. Samples with a wind direction smaller than the test's yaw rotation represent underestimations. The TSM wind direction accuracy was calculated as:

$$\boldsymbol{DE} = \frac{\mathbf{1}}{\boldsymbol{N}} \sum_{\boldsymbol{i=1}}^{\boldsymbol{N}} (\boldsymbol{\psi_{WT}} - \boldsymbol{\theta_{TSM}}) \tag{7}$$

The mean absolute direction error ($MADE$) is calculated to show how far a series of TSM wind direction estimates are from the reference regardless of over and underestimations. The $MADE$ is calculated as:

$$\boldsymbol{MA}DE = \frac{1}{N} \sum_{i=1}^{N} |\psi_{WT} - \theta_{TSM}| \tag{8}$$

where ψ_{WT} is the measured azimuth of the wind tunnel, and θ_{TSM} is the TSM wind direction estimate.

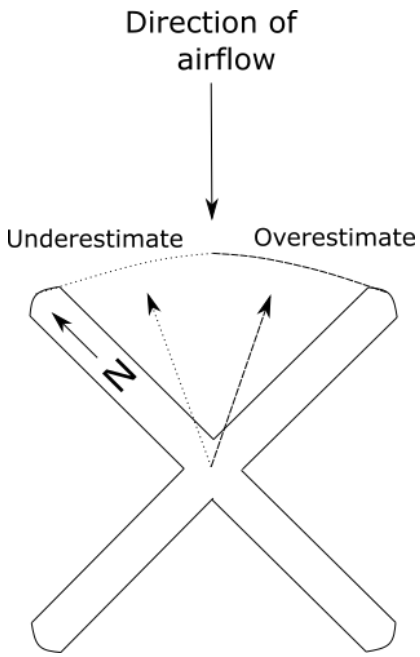

Figure 2.5: *Planview diagram showing how the wind direction observations are assessed based on the TSM estimate and mean wind direction.*

All TSM and pitot tube measurements were evaluated with a Grubb's test for outliers (α = 0.05). After testing for outliers, the difference between the TSM and pitot tube observations was calculated for each sample. Next, the ME for each test run was calculated using equation 1. The MEs were then grouped by test speed and tested for equal variances (α = 0.05) and normality with an Anderson-Darling (AD) test (α = 0.05). The RE was then calculated using equation 6. The RE samples were then tested for equal variance (α = 0.05) and normality with an AD test (α = 0.05). Last, the DE was calculated with equation 7 and tested for equal variance and normality with the same tests as the ME and RE. Because the sample size is large (n = 600), the AD test will be interpreted alongside histograms and respective skewness and kurtosis values.

Some wind tunnels can generate consistent wind speeds with little turbulence. However, the laminar airflow found in some wind tunnels is unrealistic compared to turbulent air in natural environments. Therefore, sonic anemometer calibrations completed in highly laminar airflow is not applicable to naturally turbulent airflow (Högström & Smedman, 2004). Highly laminar wind tunnels may have turbulence intensities less than 1%, whereas simple environments, such as deserts or grasslands, typically have turbulence intensities of 10% when measured 10 m above ground level (Ghanadi et al., 2017). Before testing the TSM in the wind tunnel, the airflow turbulence intensity (I_u) was measured at each test speed for five minutes. The turbulence intensity (Harper et al., 2010) was calculated to be 4.09% for all three test speeds:

$$\boldsymbol{I_u = \frac{\sigma_u}{V_{To}}} \tag{9}$$

where I_u is turbulence intensity, σ_u is the coefficient of variation for the pitot tube observations, and V_{To} is the mean wind speed.

Computational Fluid Dynamics (CFD) software (Autodesk Inc., 2018) was used to aid the visualization of different disturbances caused by the TSM structure. The 3D TSM model used in the CFD simulations was digitally reproduced from 70 overlapping photos and photogrammetry software (3D Flow, 2020).

2.3. Rotor wash assessment

A drone's rotors generate an immense amount of airflow interference. This interference disrupts the airflow around the drone and affects measurements from an onboard anemometer. To minimize the impact of rotor wash interference on the TSM, the airflow above the DJI M100 drone was measured in various locations to identify areas with minimal interference. The M100 (Figure 2.6) is a developer model that allows for customizable payload configurations and integration of other

external components. The maximum takeoff weight of the M100 is greater than the additional mass of the TSM and mounting hardware.

Figure 2.6: *The DJI Matrice 100 was used to evaluate rotor wash disturbances in this research (retrieved from https://www.dji.com/ca/matrice100).*

Because the sensors are mounted along the centerline of the drone, the rotor wash assessment focused on a two-dimensional plane above the M100. The rotor wash assessment followed a similar procedure to Alvarado et al. (2017). The test was conducted in a large barn. First, a 10 × 10 cm grid was drawn on a corrugated plastic sheet. Samples were collected at each of the intersects on the corrugated sheet. A plain view diagram of the horizontal sampling locations and rotor rotation directions is illustrated in Figure 8. Next, the M100 was mounted on a mast approximately 3 meters off the ground next to the scaffolding. This was done to avoid the phenomena known as the ground effect, where the airflow reflects off the ground and circulates back up to the rotors (Aich et al., 2014). Similarly, the scaffolding and support platforms were positioned far from the rotors to avoid interfering with the airflow. A custom extension was developed so that the TSM was positioned exactly along the centerline of the M100. The extension, visible in Figure 2.7B, is built out of a thin

ski pole to minimize disturbance. Following the test set-up, the M100 was turned on and the rotors were activated to simulate hover. The TSM was lowered into the airflow and positioned at one of the grid intersections. The TSM was held in each position on the grid for 30 seconds, while recording data. Before and after the rotor wash tests the TSM was used to measure the ambient wind speed in the barn. The TSM samples from the rotor wash test and control observations were assessed for normality and outliers with the same tests used in the wind tunnel section.

The circular standard deviation of wind direction observations (σ_θ) was calculated using the Yamartino (1984) method:

$$\sigma_\theta = arcsin(\varepsilon)\,[1 + (\tfrac{2}{\sqrt{3}} - 1)\varepsilon^3] \tag{10}$$

where ε is an estimator for standard deviation and is given by:

$$\varepsilon = \sqrt{1 - (s_a/c_a)} \tag{11}$$

where s_a and c_a are the mean $sin\,\theta$ and $cos\,\theta$ of the wind direction:

$$s_a = \tfrac{1}{n}\textstyle\sum_{i=1}^{n} sin\,\theta_i \qquad c_a = \tfrac{1}{n}\textstyle\sum_{i=1}^{n} cos\,\theta_i \tag{12}$$

where θ_i is wind direction.

Due to internal safety constraints within the DJI software, the M100 flight control software indicated that normal flight conditions were not met when fixed to the mast. When the M100 throttle was increased to hover during the fixed hover test the flight instruments cut power to the rotors as the drone's altitude was not increasing as it should have. However, if the throttle was fixed at an RPM

below the takeoff threshold the rotors would rotate at a constant rate. The test throttle was estimated to be approximately 80% of the RPM necessary for takeoff.

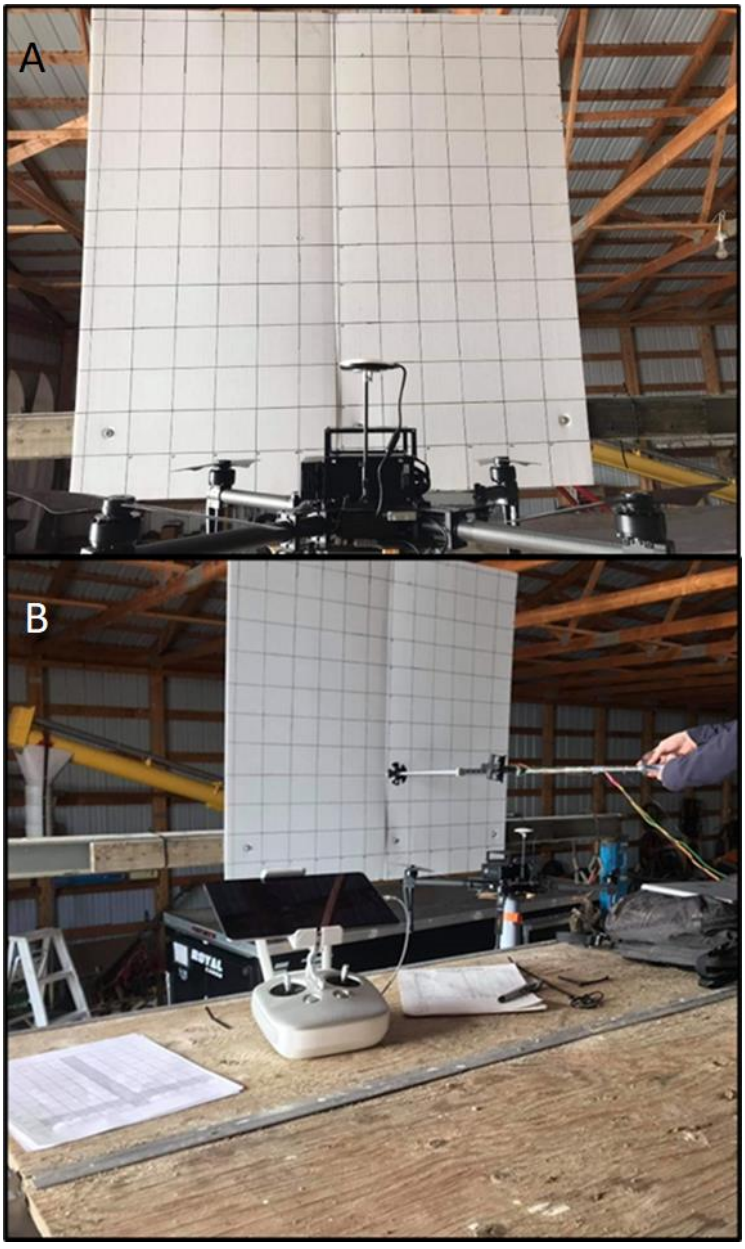

Figure 2.7: ***A)*** *Simulated hover test setup.* ***B)*** *Simulated hover test sampling procedure. All objects that could impact the rotor wash were positioned far enough to avoid interfering with the airflow.*

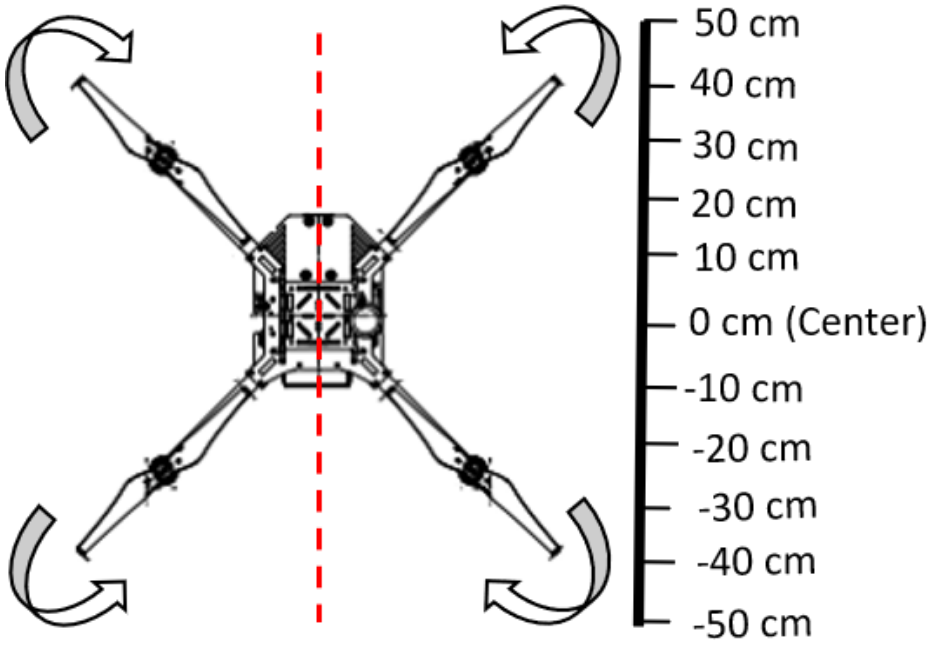

Figure 8: *Plainview diagram of the horizontal sampling pattern and M100 rotor rotation directions. Samples were collected in 10 cm intervals over the center of the drone.*

Chapter 3: Results

3.1. Overview

Testing simulated the aerodynamic environment that a sonic anemometer encounters when mounted on a multirotor drone in a broad range of flight conditions, where changes in the drone's yaw, pitch, and roll affect the orientation of the anemometer. Test results are split into two sections: wind tunnel testing (§3.1) and rotor wash analysis (§3.2). This approach was used to isolate specific sources of error and to quantify the impact they have on the TSM wind speed and direction measurements. Results indicate that errors in the TSM's wind speed and direction measurements varied depending on the sensor's pitch angle (θ), yaw rotation (ψ), and ambient wind speed. Rotor wash analysis conducted on the DJI M100 quadrotor drone identified several locations where a sonic anemometer could be mounted such that the wind speed estimate would be minimally impacted by wind generated by the rotors during hover.

3.2. Wind Tunnel Test Results

3.2.1. Pitot Tube Wind Speed Measurements

During testing, tunnel wind speed recorded by the pitot tube remained steady and did not deviate by more than 0.04 m s^{-1} from the mean values (Table 3). Each test was completed in a continuous session to rule out changes to the ambient conditions inside the facility, such as pressure-induced flows caused by opening and closing doors.

Table 3.1: *Wind speed summary statistics derived from pitot tube measurements.*

Test speed	Mean Wind Speed (m s^{-1})	Standard Deviation	Min. (m s^{-1})	Median (m s^{-1})	Max. (m s^{-1})	Range (m s^{-1})
Low	3.30	0.01	3.30	3.31	3.32	0.02
Med	9.57	0.01	9.56	9.58	9.60	0.04
High	13.93	0.02	13.89	13.93	13.97	0.09

3.2.2. TSM Wind Speed and Direction Measurements

Conventionally, sonic anemometers are mounted in fixed horizontal positions so that the sensor is aligned with the ambient airflow along a flat plane. Large angles of attack relative to the horizontal wind vector can cause significant distortions to a sonic anemometer's wind speed and direction estimate (Wilczak et al., 2001). As such, samples where the TSM pitch angle (θ) was set to 0° and thus aligned with the mean streamline airflow (θ = 0°) are examined first. Positive mean error (ME) values indicate the TSM recorded higher wind speed than the pitot tube, and vice versa for negative ME values. These tests eliminate the impact of angle of attack errors while highlighting errors related to transducer shadowing. Testing began with a yaw rotation of 0° where the North strut was parallel to the wind tunnel, followed by counterclockwise rotations at 10° increments up to 90° (n = 30). A full record of the pitot tube and TSM wind speed and direction measurements are provided in Appendix A.

Testing the effects of yaw rotation with a fixed pitch angle showed that the highest MAE for all three test speeds was recorded at 0° yaw rotation, corresponding to the position where the North transducers and vertical support strut were aligned with the axis of the wind tunnel (Figure 3.1A). Other notable errors occurred at ψ = 50° and 70°, corresponding to yaw rotations where airflow entering the TSM's measurement area was minimally affected by the struts or transducers. Overall, the greatest RE values relative to the test wind speeds were at ψ = 0° and 70°. RE values also indicate that

the TSM consistently under-estimated wind speed in the low-speed test runs, while it both under- and over-estimated wind speed in the medium- and high-speed test runs.

Variability in the wind speed recorded by the TSM increased with test speed and peaked at $\psi = 70°$. It is important to note that the wind speed variations were similar between samples at 0° and 90° yaw rotations, but the ME and RE values were not, even though vertical support struts were aligned with the tunnel at both rotations. The key difference that may explain these results is that at 90° yaw rotation the West transducer facing into the wind is located on the lower portion of the sensor body, whereas at 0° yaw rotation the North transducer is located on the upper portion of the sensor body. It is unclear why this difference manifests, but it suggests that the error is not symmetric and that small changes in the position of transducers affect the accuracy of wind speed measurements with the TSM in a static mounting position.

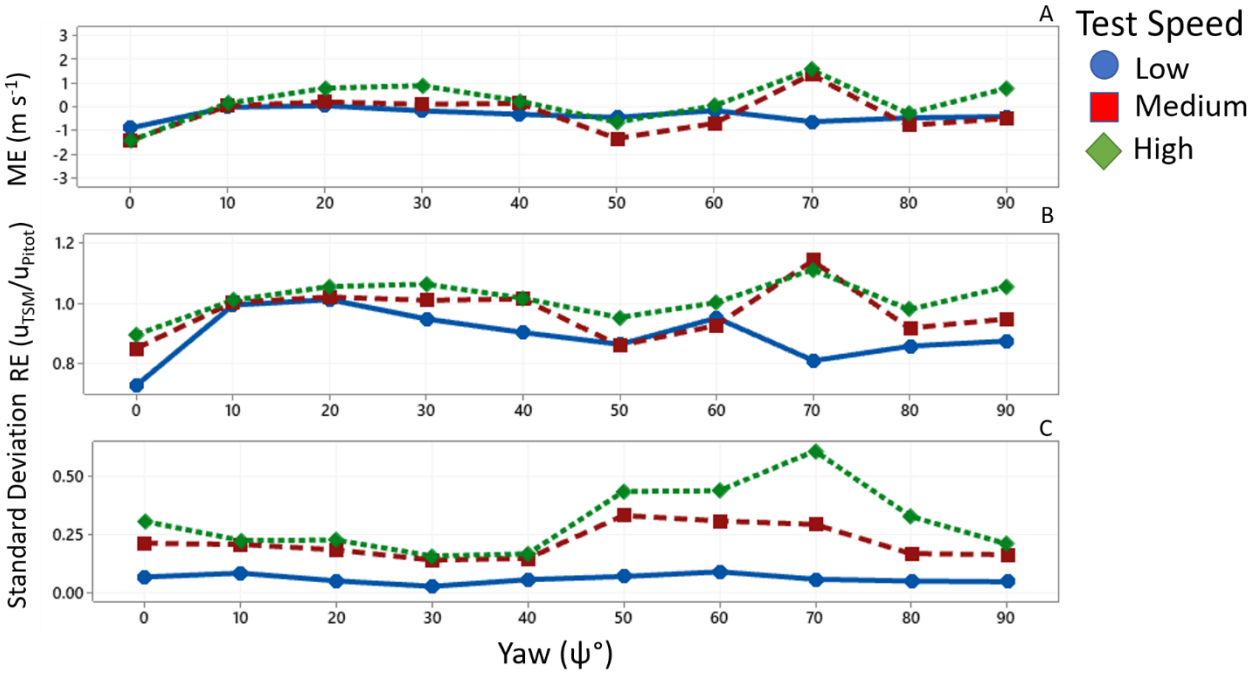

Figure 3.1: ***A)*** *TSM wind speed ME recorded during each test speed (ψ = 0° to 90°, θ = 0°, n = 30).* ***B)*** *TSM wind speed RE recorded during each test speed (ψ = 0° to 90°, θ = 0°, n = 30).* ***C)*** *Standard deviation of ME at each yaw rotation for each test speed (ψ = 0° to 90°, θ = 0°, n = 30).*

Very few samples collected while the TSM was mounted at θ = 0° met the manufacturer's specifications. The low- and medium-speed tests (3.3 m s^{-1}, 9.6 m s^{-1}) fall within the low-speed accuracy category according to the manufacturer (0 – 10 m s^{-1}) and should be within 0.1 m s^{-1} of the true wind speed according to specifications. The high-speed test (13.9 m s^{-1}) is categorized as a medium-speed wind by the manufacturer (11 – 30 m s^{-1}) and should be accurate to within 1% of the true wind speed according to specification. The *MAE* observed for samples collected with no angle of attack (θ = 0°) was 0.35 m s^{-1} in the low-speed test (*n* = 10), and 0.66 m s^{-1} in the medium-speed test (*n* = 10) (Figure 3.1A). The *MAE* recorded during the high-speed test was only accurate to within 5% or 0.68 m s^{-1} of the reference (*n* = 10) (Figure 3.1 B). Only six of thirty samples from all test speeds collected with zero angle of attack (θ = 0°) met the stated accuracy levels. Notably, all three samples

collected with a yaw rotation of 10° were consistently closest to the reference wind speed measured by the pitot tube.

Wind speed measurement errors associated with changes in TSM pitch angle or angle of attack are presented in Figure 3.2. In this set of test runs, pitch varied from +30° to -30°. For context, positive pitch is when the top of the TSM is tilted backward or away from the wind and negative pitch is when the top of the TSM is tilted forward into the wind. Yaw was held constant ($\psi = 0°$) such that the North support strut and upper transducer were aligned with the wind in all test runs ($n = 21$). Overall, MAE values were substantially larger than in the test runs with a fixed pitch angle (0°) and yaw rotations spanning 0 – 90°. MAE values increased with positive pitch angles (Figure 3.2A). The largest MAE for each test speed occurred at $\theta = +30°$. There is a marked increase in the MAE values at positive pitch angles for medium- and high-speed test runs, as well as increased variability (Figure 3.2B). MAE values for negative pitch angles were much lower than the positive angles and closer to zero. Differences in the MAE values for different test speeds were also much lower. A weak to moderate negative relation between the ME and pitch angle was identified using a Pearson's correlation ($\alpha = 0.10$) for the medium- ($n = 70$, $r = -0.35$, $p < 0.01$) and high-speed tests ($n = 70$, $r = -0.44$, $p < 0.01$). Thus, while the correlation is not very strong, the effect of pitch angle on the TSM-measured wind speed is stronger than the effect from yaw rotations.

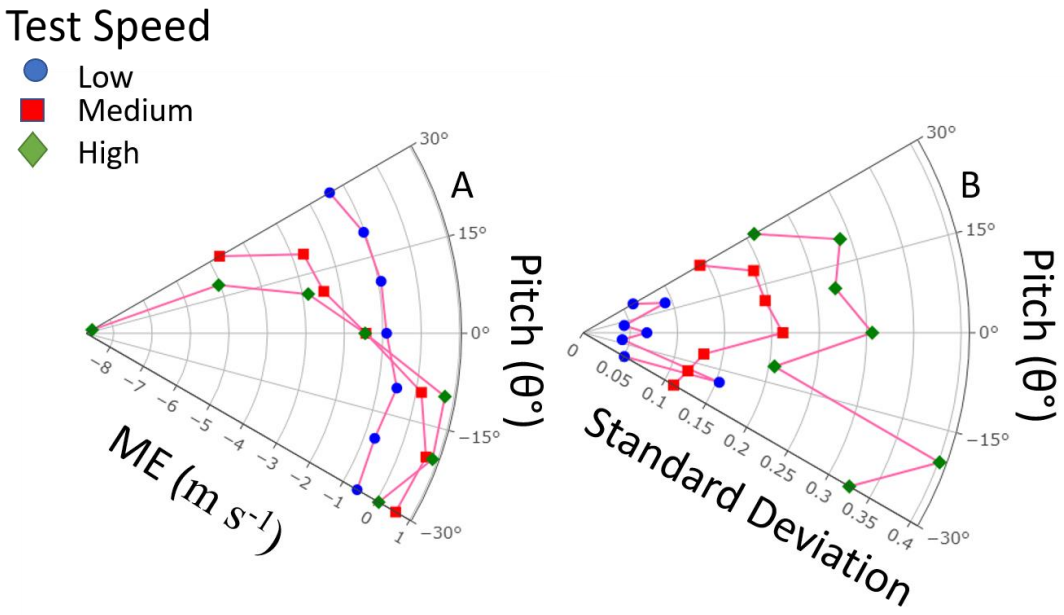

Figure 3.2: ***A)*** *ME recorded at each pitch angle for each of the three test speeds (ψ = 0°, θ = 30° to -30°, n = 21).* ***B)*** *Standard deviation of ME at each pitch angle for each test speed (ψ = 0°, θ = 30° to -30°, n = 21).*

Compared to the manufacturer's specifications, the effects of pitch angle are pronounced. However, the tests conducted at pitch angles of ±20° and ±30° exceed the manufacturer's maximum angle of attack (±15°). These tests were included to analyze the impacts of steep angles of attack that could be encountered by a modern multirotor drone. The ME for tests that fell within the manufacturer's specifications for maximum angle of attack are shown in Figure 3.3. In the medium- and high-speed tests, samples collected with no pitch angle were bounded by the -10° test above, and the 10° test below. Observations from tests with pitch angles that fell within the manufacturer's specifications (θ = 0°, ±10°) were closer to the reference instrument than tests with pitch angles that exceeded the maximum positive angle of attack ($\theta \geq 20°$). Conversely, the ME for tests with pitch angles that exceeded the maximum negative angle of attack ($\theta \leq -20°$) were similar to the ME

recorded for tests within the manufacturer's specifications. These results indicate that negative pitch angles have a smaller impact on the wind speed estimate than positive angles.

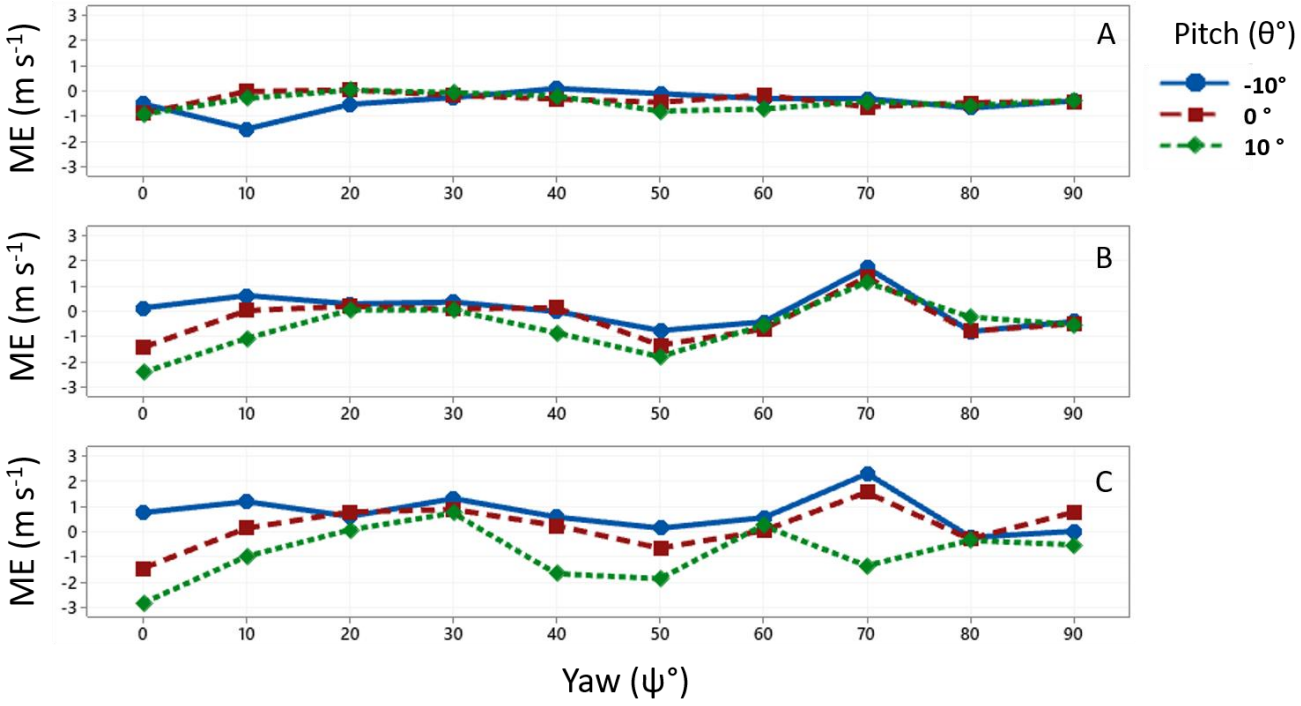

Figure 3.3: *ME recorded during tests that fell within the manufacturer's specification on the maximum angle of attack ($\theta \leq 15°$, $\theta \geq -15°$).* ***A)*** *Low speed ME (n = 21).* ***B)*** *Medium-speed ME (n = 21).* ***C)*** *High-speed ME (n = 21).*

One of the factors that may account for the large difference in ME values between positive and negative pitch angles is the experimental setup. A small plate securing the TSM to the ball mount may have disrupted airflow along the base of the sensor before it entered the measurement area at positive pitch angles, so the measurements may have been affected by the mount design (Figure 3.4). This effect appears to have been more prominent than interference from the top of the sensor body at negative pitch angles. The TSM was purposely overhung on the leading edges of the mounting plate to limit potential interference caused by the hardware. Despite the potential bias the setup may have

induced, the measurements are still useful because there are a range of mounting scenarios on drones that could impact wind speed measurements according to pitch angle. For example, the manufacturer's website presents images showing many different mounting configurations on drones. So, while the experimental setup used in this study may have created a bias and led to larger errors at positive pitch angles, the aerodynamic effects of different mounting configurations used on drones should be expected to produce similar biases.

Figure 3.4: *TSM attached to the ball mount during testing. The TSM was positioned so the sensor was slightly overhanging the leading edge of the mounting plate.*

TSM wind direction error (DE) was first examined for a constant pitch angle ($\theta = 0°$) while the sensor was rotated at 10° increments from 0 – 90° based on measurements with the IMU. DE is the

average difference in degrees between the TSM-measured wind direction and the direction determined by the IMU. Negative DE values indicate TSM wind direction < yaw rotation. Noting that the TSM was rotated counterclockwise, a yaw rotation of 10° corresponds to a wind direction of 10° if the TSM measurements have no error. A negative DE indicates the TSM-recorded wind direction was less than the yaw rotation, and vice versa for a positive DE. Results in Figure 3.5 show that the highest *DE* occurred in the low-speed tests, with large error values at yaw rotations of 20° and between 70 – 90°. *DE* was lower in the medium- and high-speed tests. A Pearson's correlation ($\alpha = 0.10$) indicates a relatively strong positive relationship between DE and yaw rotation ($n = 70$, $r = 0.76$, $p < 0.01$). The manufacturer's specifications indicate the TSM wind direction estimates are accurate to ±1° when the sensor's angle of attack is less than ±15° relative to the horizontal streamline flow. When the TSM was level with the horizontal flow in the wind tunnel, the $MADE$ recorded were 2.9° and 2.3° during the medium- and high-speed tests ($n = 10$). Low-speed tests resulted in a larger error as the $MADE$ was 7.7° ($n = 10$). As such, these tests do not reproduce the manufacturer's stated accuracy.

A second set of tests were conducted to examine DE when the yaw rotation was fixed but the pitch varied from +30° to -30° (Figure 3.6). In this configuration, one of the upper transducers and one of the vertical support struts were aligned with the tunnel axis while the pitch varied. A DE of zero is expected if the TSM measurements are perfectly accurate. Negative DE values indicate direction left error (< 360°), while positive DE values indicate a right error (> 0°). Results in Figure 3.6A show mostly negative DE values for the low-speed test runs, indicating a left bias in recorded wind direction, but for all test speeds the largest DE and standard deviation occurred at $\theta = +30°$, which may indicate airflow disruption from the base of the sensor or the base plate holding the TSM to the ball mount. DE values were small and did not vary greatly for the medium- and high-speed test runs from -30° to +10°. Pearson correlation coefficients indicate a weak negative relation between DE and pitch angle in the low-speed test ($n = 21$, $r = -0.30$, $p = 0.01$), and slightly stronger negative

relationships for the medium- (n = 21, r = -0.41, p < 0.01) and high-speed tests (n = 21, r = -0.51, p < 0.01).

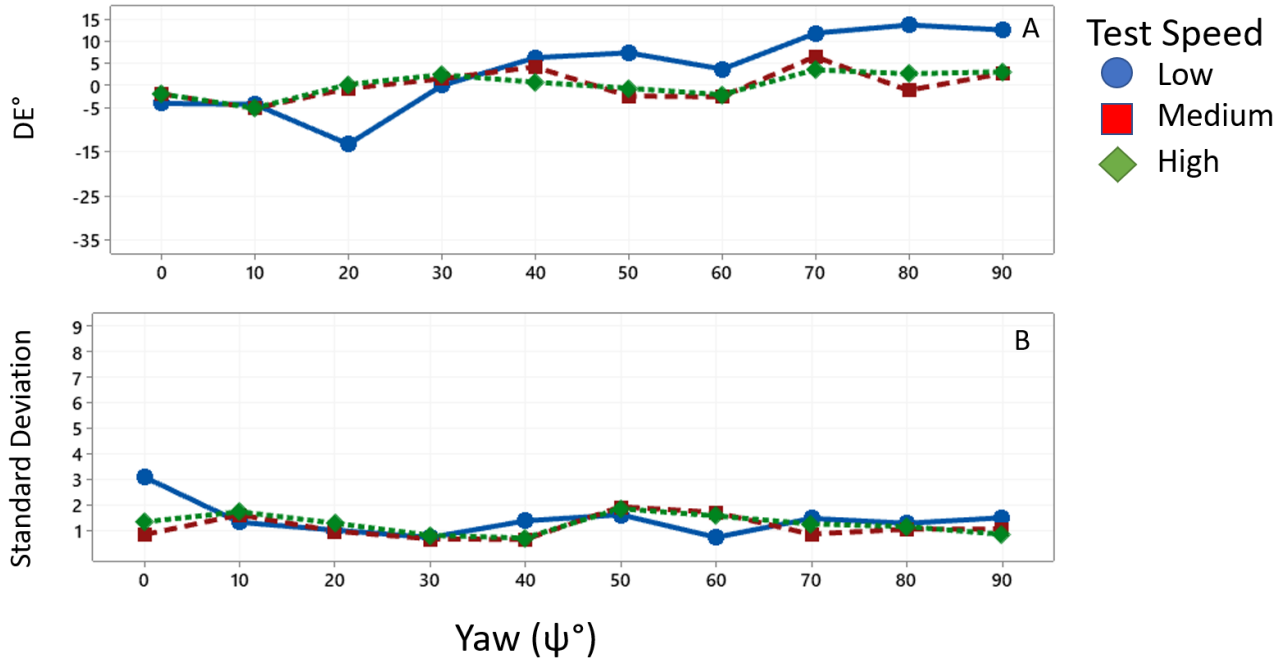

Figure 3.5: ***A)*** *Directional error (DE) recorded at each yaw rotation for each test speed (ψ = 0° to 90°, θ = 0°, n = 30).* ***B)*** *Standard deviation of DE recorded at each yaw rotation (ψ = 0° to 90°, θ = 0°, n = 30).*

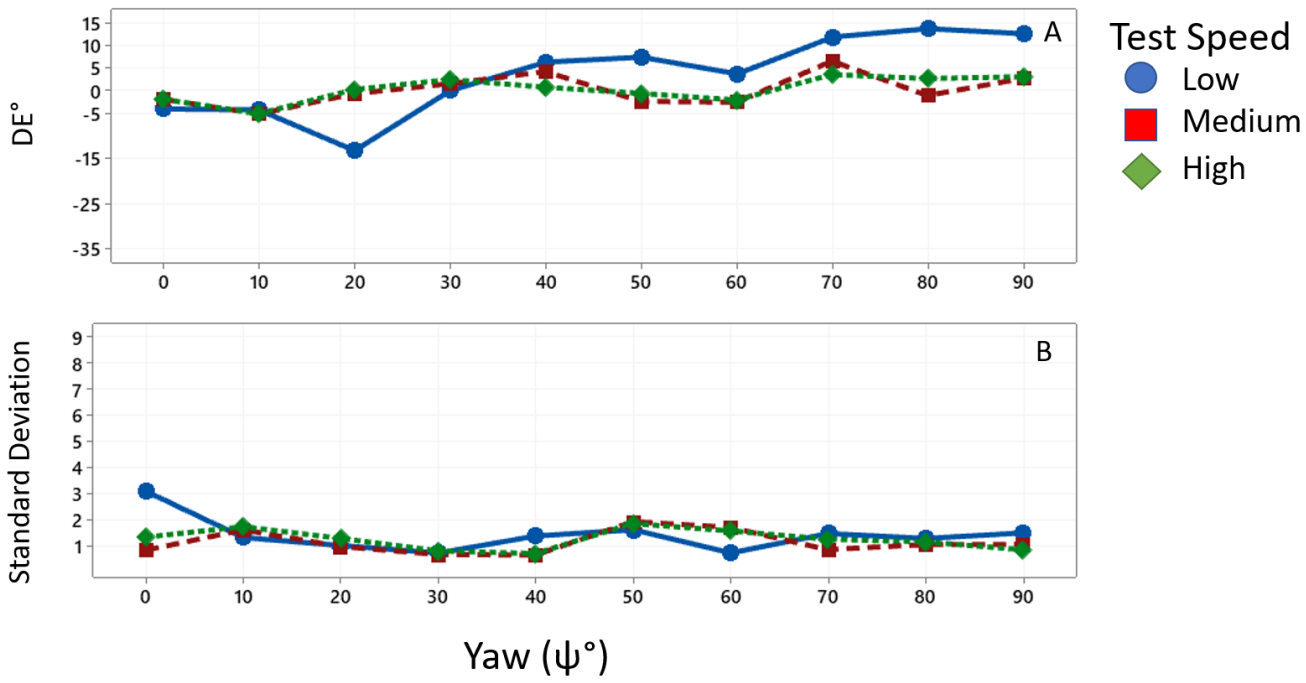

Figure 3.6: ***A)*** *DE recorded at each pitch angle for each test speed (ψ = 0°, θ = 30° to -30°, n = 21).* ***B)*** *Standard deviation of DE for each pitch angle for each test speed (ψ = 0°, θ = 30° to -30°, n = 21).*

As mentioned, some of the pitch angles that were tested exceeded the manufacturer's maximum angle of attack (±15°). The DE for samples collected within the manufacturer's specification are shown in Figure 3.7. In the medium- and high-speed tests there was little variability between the samples taken at different pitch angles. Whereas, in the low-speed test there were larger variations between samples taken at different pitch angles. TSM wind direction observations from tests that were within the manufacturer's specifications for maximum angle of attack had $MADE$ values of less than ±4° in the medium- and high-speeds. Generally, the DE for tests within the manufacturer's specifications were smaller than tests with steep positive pitch angles ($\theta \geq 20°$). However, the DE recorded during tests with steep negative pitch angles ($\theta \leq 20°$) were close to the DE

observed between pitch angles between 10° and -10°. Similar to the impact of positive and negative pitch angles on ME, steep negative pitch angles have a smaller influence on DE than steep positive pitch angles.

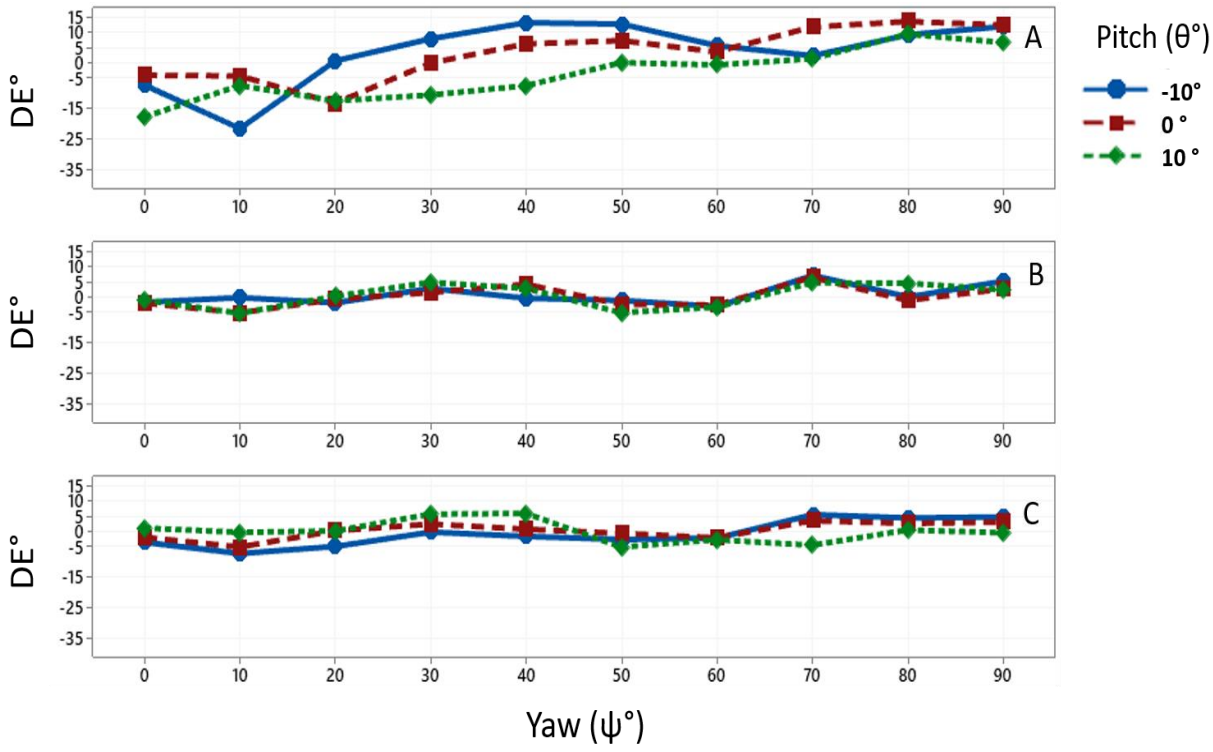

Figure 3.7. *DE recorded during tests that fell within the manufacturer's specification on the maximum angle of attack ($\theta \leq 15°$, $\theta \geq -15°$).* ***A)*** *Low-speed DE.* ***B)*** *Medium-speed DE.* ***C)*** *High-speed DE.*

The wind speed relative errors (RE) for different combinations of pitch and yaw are shown in Figure 3.8. RE values below unity indicate the TSM under-estimated wind speed, corresponding to 92% of the low-speed tests. Conversely, TSM wind speed over-estimations occurred in 38% and 63% of all test runs for medium- and high-speed tests, respectively. Overall, Figure 3.8 shows a transition from under-estimation to over-estimation as test speed increased for all combinations of pitch and

yaw. The largest TSM wind speed under-estimations for all tests speeds occurred at high positive pitch angles and low yaw rotations, although there is one exception in the low-speed tests where the largest under-estimation occurred at a $\psi = 10°$ and $\theta = -10°$. The greatest TSM wind speed over-estimations occurred in the high-speed tests at high yaw rotations and negative pitch angles. In the medium-speed tests, the largest over-estimations occurred across pitch angles from +10° to -30° when the yaw rotation was 70°. In all test speeds, there is a general trend of increasing RE values from positive to negative pitch angles at $\psi = 0°$.

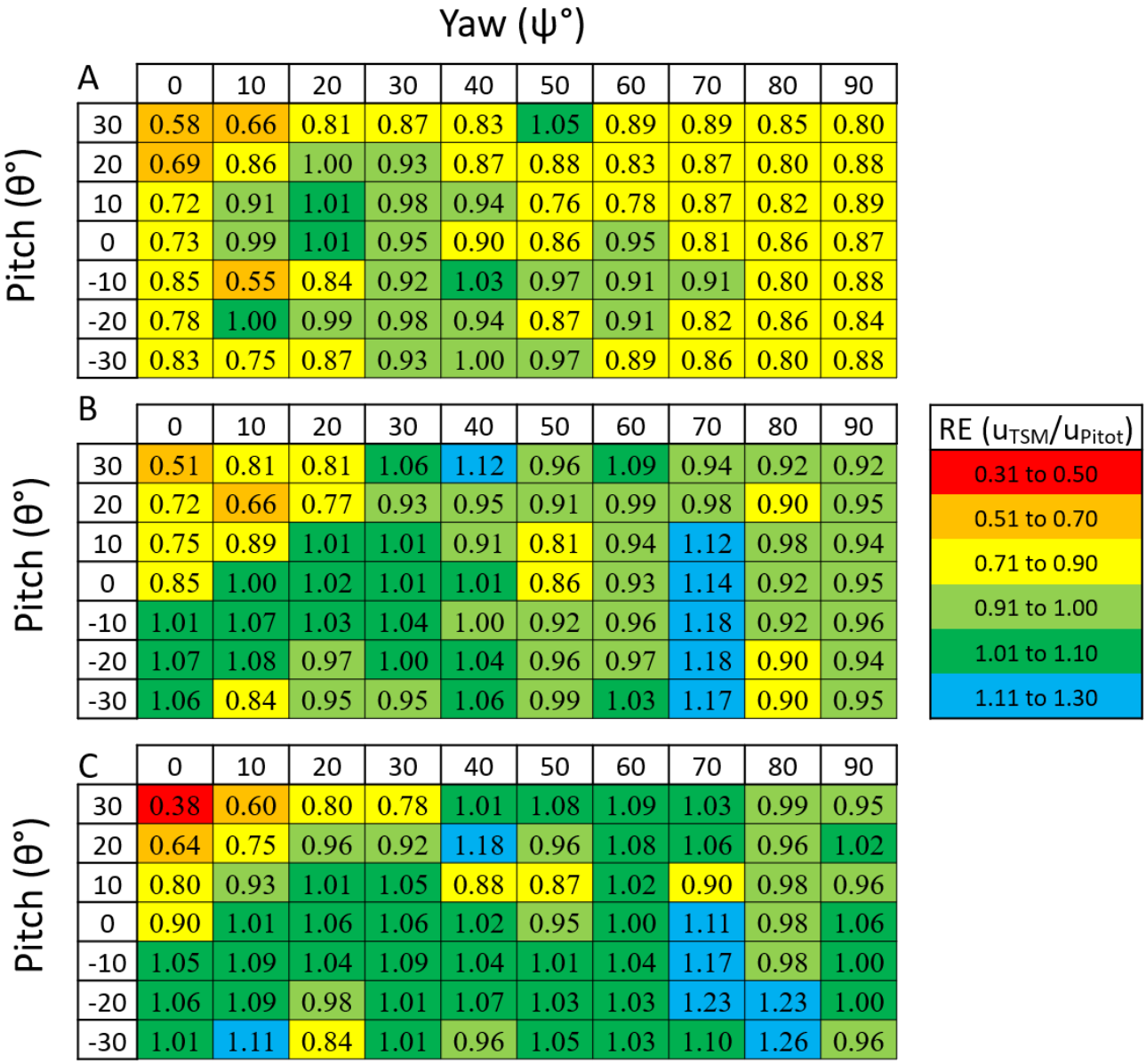

Figure 3.8: *Wind speed relative error (RE) for different test speeds:* ***A)*** *Low-speed (3.3 m s^{-1}),* ***B)*** *Medium-speed (9.6 m s^{-1}), and* ***C)*** *High-speed (13.9 m s^{-1}).*

The wind direction errors (DE) for different combinations of pitch and yaw are shown in Figure 3.9. In the low-speed tests (Figure 3.9A), the pattern shows a dominance of negative error in the top left and a dominance of positive error in the bottom right. This suggests a transition in the sign of the error as yaw rotation increased up to 90° and as pitch transitioned to negative angles. The same

pattern does not appear to manifest for the medium- and high-speed tests. In all test speeds, the largest change in DE occurred across 0 – 90° yaw rotations at +30° pitch, suggesting high positive pitches have the most influence on DE. In contrast, more positive DE values occurred at negative pitches for the medium- and high-speed tests. This could be caused by the transducer layout as the largest positive DE values occur when the sensor is rotated so the West support strut and lower transducer were aligned with the wind tunnel.

Yaw (ψ°)

A	0	10	20	30	40	50	60	70	80	90
30	-22.93	-5.20	-11.68	-14.33	-15.19	-0.13	-1.66	-1.74	4.39	8.06
20	-0.93	-6.99	-10.60	-13.41	-5.79	-3.78	2.40	1.57	8.89	3.95
10	-17.76	-7.41	-12.47	-10.55	-7.47	0.15	-0.62	1.43	9.55	6.82
0	-4.04	-4.24	-13.26	0.01	6.33	7.43	3.72	11.89	13.73	12.61
-10	-7.31	-21.53	0.66	7.88	13.14	12.66	5.58	2.32	9.19	11.90
-20	-17.00	-7.02	-6.83	-0.96	5.18	4.21	5.85	12.44	14.64	12.97
-30	-1.29	-14.89	-11.22	-1.31	6.81	5.40	5.96	3.48	13.07	7.50

Pitch (θ°)

B	0	10	20	30	40	50	60	70	80	90
30	-33.68	-0.62	0.90	-18.78	-17.51	-13.47	-6.43	-6.34	-5.13	1.02
20	-2.05	-9.98	10.62	9.06	2.64	-6.29	-5.09	-1.22	-4.04	3.37
10	-0.85	-5.23	0.38	4.98	2.95	-5.05	-3.19	4.81	4.68	2.51
0	-1.86	-5.13	-0.60	1.61	4.31	-2.32	-2.52	6.64	-1.02	2.79
-10	-1.68	-0.17	-1.87	2.84	-0.37	-1.11	-3.04	7.11	0.05	5.25
-20	-0.28	9.30	8.94	0.88	-5.12	-3.91	-3.93	7.90	1.47	4.39
-30	1.23	10.71	15.31	3.25	-8.33	-9.00	-1.68	7.93	1.13	5.94

Pitch (θ°)

C	0	10	20	30	40	50	60	70	80	90
30	-26.24	4.52	7.91	7.93	-10.44	-7.54	-1.86	2.19	3.01	4.14
20	-16.56	-9.56	5.40	7.08	-5.80	-8.29	-3.66	-0.77	-0.04	3.64
10	1.22	-0.19	0.26	5.80	6.06	-5.08	-2.64	-4.46	0.56	-0.31
0	-1.84	-5.05	0.31	2.53	0.83	-0.54	-2.02	3.65	2.74	3.18
-10	-3.58	-7.23	-4.91	-0.22	-1.63	-2.65	-2.14	5.51	4.41	4.76
-20	-2.33	8.73	17.98	3.88	1.71	3.03	0.47	8.96	18.96	15.87
-30	0.69	11.42	21.66	22.10	8.07	2.19	3.23	10.58	18.72	10.09

DE°
-35 to -26
-25 to -16
-15 to -11
-10 to -6
-5 to -1
-1 to 1
1 to 5
6 to 10
11 to 14
15 to 25

Figure 3.9: *Wind directional error (DE) for each test speed:* ***A)*** *low (3.3 m* s^{-1}*),* ***B)*** *medium (9.6 m* s^{-1}*),* ***C)*** *high (13.9 m* s^{-1}*).*

The following points summarize the main results and interpretations from wind tunnel testing the relative accuracy of the TSM at different yaw rotations and pitch angles:

a. The pitot tube measurements indicate the tunnel wind speed was steady, with no more than 4.09% deviation from the mean at each test speed level. The variations in wind speed

measurements recorded by the pitot tube are much smaller than the variations noted in the TSM over the range of yaw rotations and pitch angles tested.

b. TSM wind speed measurement error varied with yaw rotation. The largest error, which corresponded to a wind speed under-estimation by the TSM, occurred when one of the upper transducers and vertical support struts were aligned with the wind tunnel ($\psi = 0°$). However, the error was not reproduced at $\psi = 90°$, where the lower transducer and vertical support were aligned with the wind tunnel. This suggests a small design effect on measurement accuracy caused by transducer placement.

c. TSM wind speed measurement errors were more pronounced with changes in pitch compared to changes in yaw rotation, particularly at positive pitch angles and zero yaw rotation when the top of the TSM is tilted backwards away from the tunnel. In this configuration, one of the upper transducers and one of the vertical support struts was aligned with the tunnel. The base plate used to secure the TSM to the ball mount may have interfered with the flow before it entered the measurement area. However, this interference is likely representative of different mounting configurations used on drones, as evidenced by images on the manufacturer's website.

d. Testing was unable to reproduce the manufacturer's stated measurement errors at different test speeds. Generally, this study showed that the TSM error is greater than the values stated by the manufacturer. Although the manufacturer does not recommend pitch angles > 15°, results showed that wind speed measurement error can be quite low at steeper pitch angles depending on the yaw rotation.

e. The TSM wind speed measurement error varied by test speed. The sign and magnitude of wind speed error varied for different combinations of yaw rotations and pitch angles. In

low-speed tests, the TSM generally under-estimated wind speed, while in high-speed tests it generally over-estimated wind speed.

f. In general, steep pitch angles had the greatest effect on TSM wind direction measurement error, but tests showed that large direction errors could also manifest, though less commonly, at lower pitch angles.

3.2. Rotor Wash

The rotor wash analysis was used to map the rotor-induced horizontal wind speed on a two-dimensional plane projecting above the drone center. During testing the ambient wind speed inside the test enclosure was 0.20 m s^{-1}, with a standard deviation of 0.08 ms^{-1}. The wind speed measurements were taken along a two-dimensional plane over the center of the drone. The measurement region extends 10 cm beyond the rotors on both sides.

The mean wind speed for each sampling location was calculated and plotted to visualize the change in horizontal wind speed (Figure 3.10). The highest wind speeds induced by the rotors was not recorded directly above the rotors. Instead, the highest wind speeds occurred on the leading edge of the front rotor and the trailing edge of the rear rotor. High levels of disturbance at the tips of rotors has been noted in other research (Donnell et al., 2018). Interference caused by the rotors progressively lost energy radially as the vertical or lateral distance increased. Several pockets of turbulent air were located directly above the centerline of the M100 approximately 20 cm from each other. Positioning a sonic anemometer at least 50 cm above the M100 rotors reduces the impact of rotor-induced airflow in calm wind conditions. Increasing the anemometer's position above 50 cm does not appear to be beneficial.

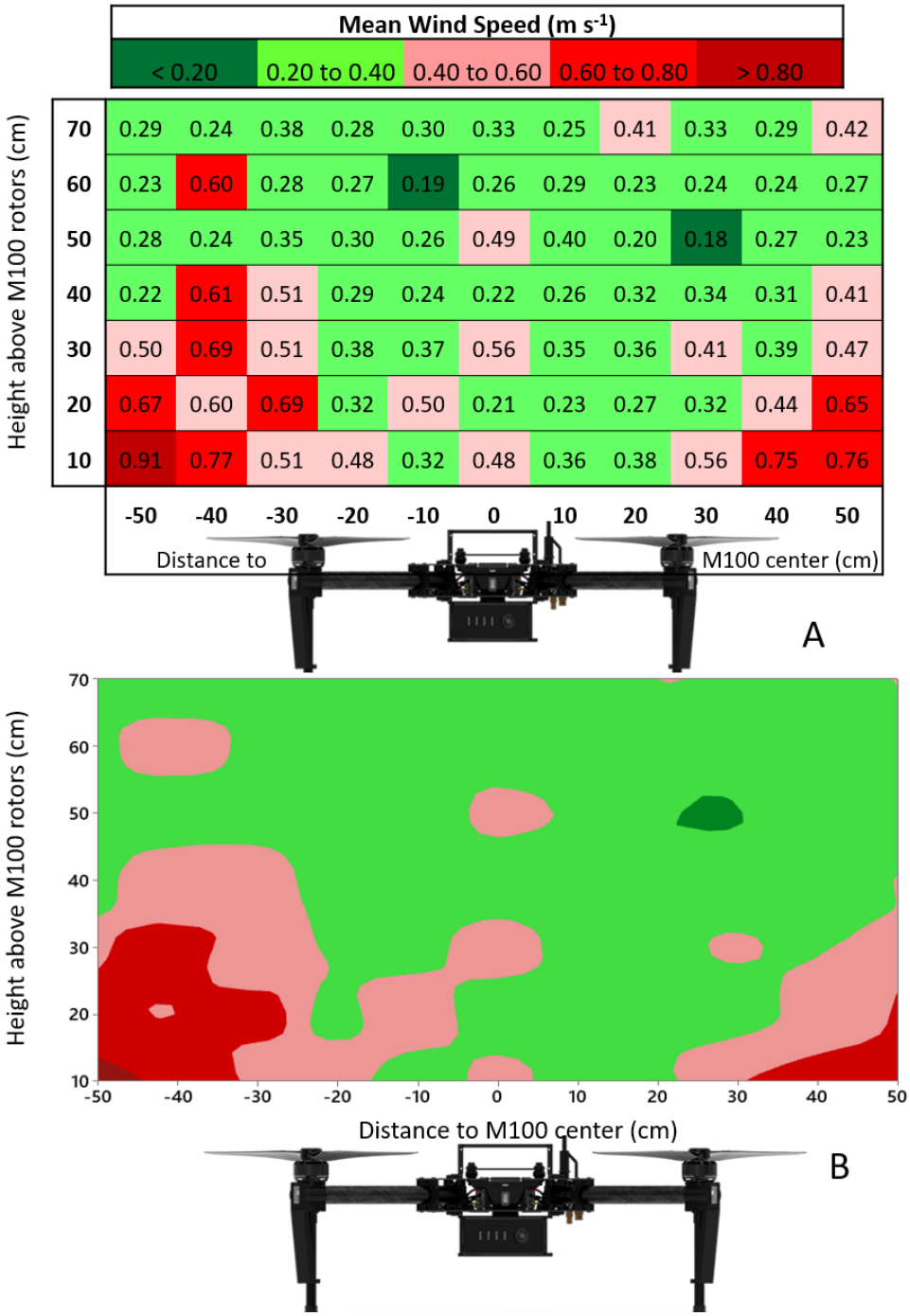

Figure 3.10: *Gridded **(A)** and contour plot **(B)** of mean horizontal wind speed (m s^{-1}) recorded at each vertical and lateral position above the center of the M100 drone while the rotors were spinning.*

The standard deviation of wind speeds does not follow the same radial pattern in relation to the rotors as mean wind speed (Figure 3.11). Instead, the largest cluster of high standard deviations was found 30 cm above the rotors extending 40 cm behind the center to 20 cm in front of the center point. The low standard deviations recorded near the rotors was likely caused by consistent downward airflow generated by the rotors.

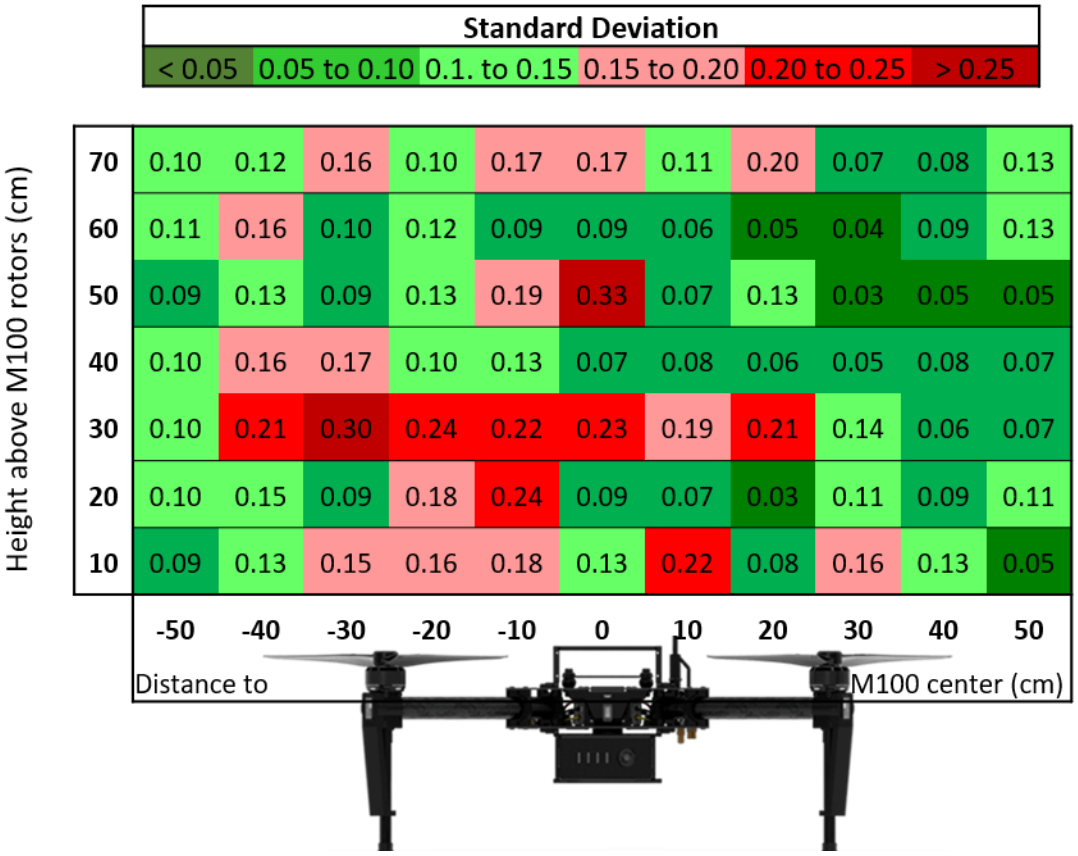

Figure 3.11: ***S****tandard deviation of wind speed recorded at each vertical and lateral position above the center of the M100 drone while the rotors were spinning.*

The airflow interference generated by the M100 rotors appears to drastically influence the apparent wind direction depending on the sampling location. The chart in Figure 3.12 shows the mean two-dimensional wind direction recorded by the TSM at each sampling location while the rotors were spinning compared to the mean wind direction measured when the drone was shut off (herein:

control). The mean wind direction observed during the control was from 334° with a standard deviation of 18°. The drone was aligned north to south with the front pointing towards the north, meaning the ambient airflow was from 26° to the left of the drone (Figure 3.12).

Samples taken over the front half of the drone had similar wind directions compared to the control. Conversely, samples taken over the rear of the drone were sporadic and generally display a tailwind. However, a sample's height above the front rotors does not appear to influence the wind direction observations as much as with wind speed. The wind direction's standard deviation follows a similar pattern in terms of lateral sampling location (Figure 3.13). The standard deviation of wind direction observations over the front half of the M100 were generally lower than their rear counterparts. The lowest standard deviations recorded in front and behind the drone occurred close to rotors where the highest induced wind speeds were also recorded.

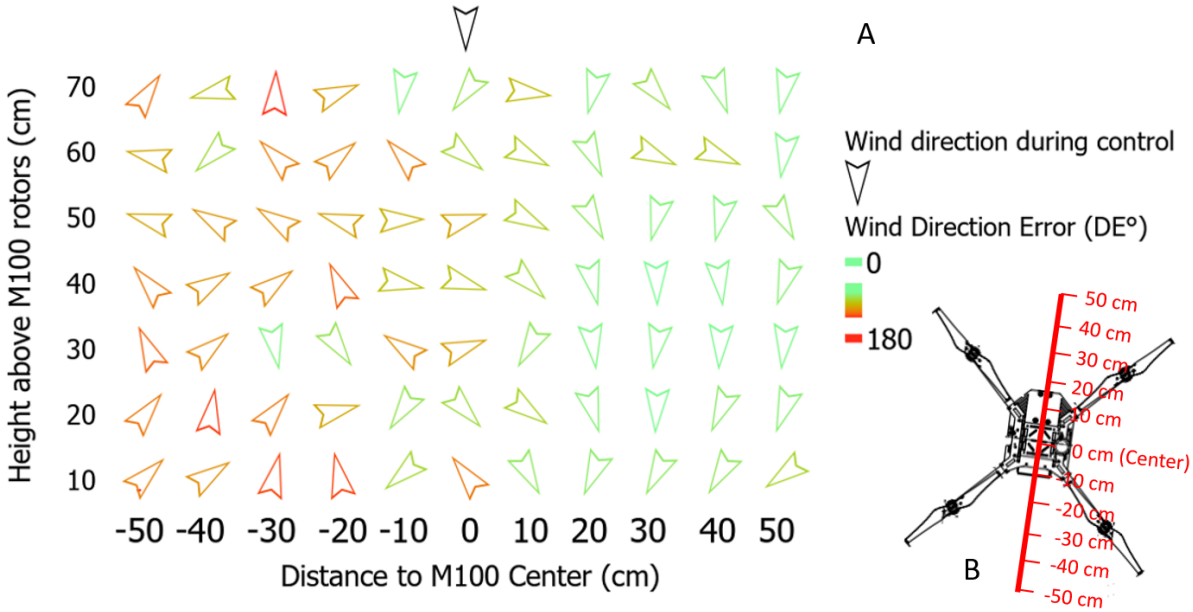

Figure 3.12: ***A)*** *Mean wind directions recorded at each sampling location. Each arrow is a mean two-dimensional wind direction from the TSM.* ***B)*** *Top-down diagram of the M100's heading relative to the mean wind direction recorded during the control test and lateral sampling locations.*

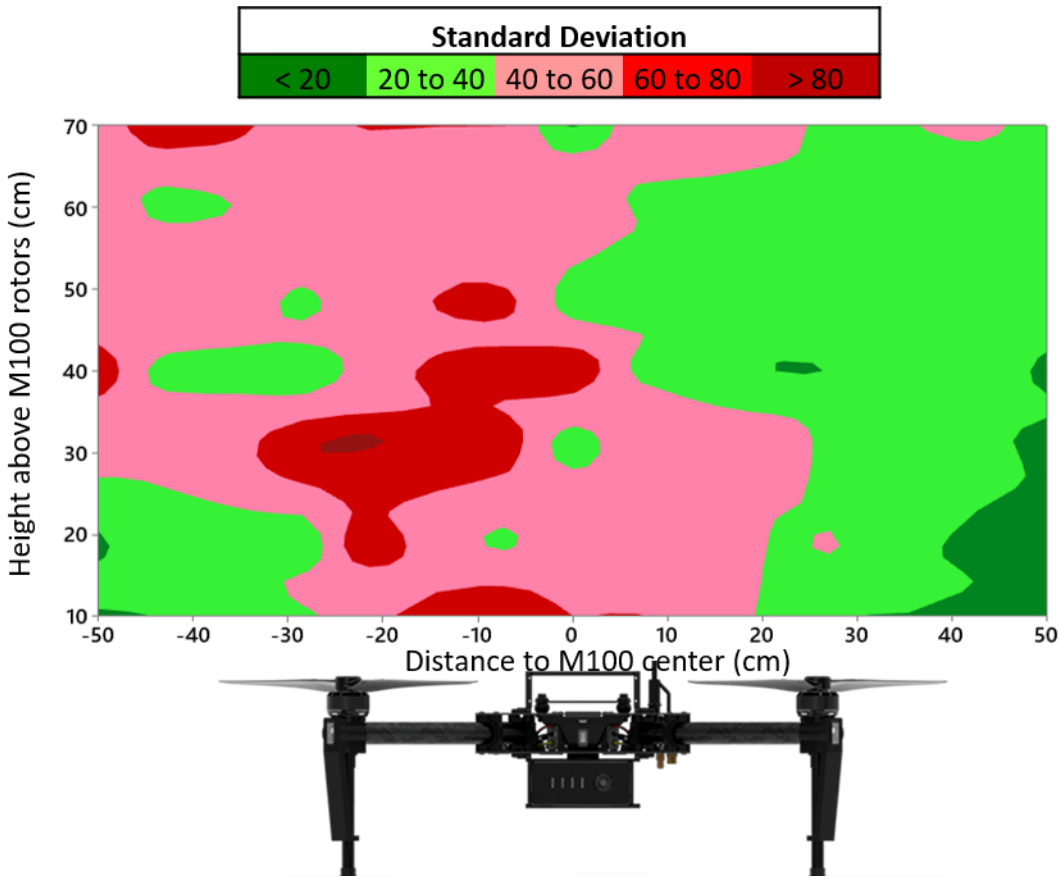

Figure 3.13: *Standard deviations of wind direction observations recorded at each vertical and lateral position above the center of the M100 drone while the rotors were spinning.*

Mounting a sonic anemometer on a multirotor drone requires careful placement to minimize the impact of rotor-induced airflow. Both wind speed and wind direction estimates could be affected if the anemometer is not located out of the rotor wash interference. The following points summarize the main results of the rotor wash analysis:

A. The induced airflow directly above the center of the rotors was not necessarily the highest. The highest recorded induced wind speeds occurred above the leading edge of the front rotor, and the trailing edge of the rear rotor. However, rotor-induced airflow dissipated radially as the vertical or lateral distance increased.

B. The standard deviation of the wind speed samples did not follow the same radially dissipating trend. Instead, the standard deviation of wind speed samples collected 30 cm above the rotors were somewhat similar. At or below 30 cm above the rotors resulted in highly variable samples.

C. Wind direction estimates appear to be more impacted by induced airflow near the rear of the M100. Whereas samples taken near the front of the drone appear to be less impacted. A sample's height above the front rotors does not appear to influence wind direction estimates as much as wind speed.

D. The standard deviation of wind direction observations was lower for samples taken near the front of the M100. Conversely, the wind direction variance was much higher near the back of the drone. These results indicate the wind direction is less variable near the front of the drone.

E. A TSM mounted on an M100 multirotor should be positioned at least 50 cm above the rotors to minimize the impact on wind speed observations and towards the nose of the drone to mitigate wind direction errors. Similar research conducted on equally large multirotors found minimal wind speed interference at the same height above the rotors (Shimura et al., 2018).

Chapter 4: Discussion

4.1. Overview

The low mass of miniaturized sonic anemometers like the TSM allow these sensors to be fixed to small modern multirotor drones. The combination of these two technologies could create novel methods of measuring meteorological and atmospheric parameters from a mobile observer. However, the results of this research and other studies demonstrate that the aerodynamic environment created by a multirotor drone in flight makes collecting accurate wind speed and direction data challenging (Smith et al., 2016; Hollenbeck et al., 2018; Hollenbeck, et al., 2019). This research focused on identifying potential sources of error that could impact the accuracy of a miniaturized sonic anemometer mounted on a multirotor drone. Angle of attack errors and transducer shadowing were shown to significantly distort the wind speed and direction estimate depending on the TSM's pitch angle and yaw rotation relative to the mean wind direction. However, an alternative anemometer model would be impacted differently by the sources of error tested in this research. The rotor wash generated by a multirotor drone in simulated flight creates a significant amount of interference around the aircraft. Despite the high level of chaotic energy caused by the rotors, testing has shown there are regions above the body of a multirotor drone that could be suitable for measuring wind speed and direction while hovering. Similar to the anemometer-specific errors, different multirotor drone models will create different zones of interference.

4.2. Wind Tunnel Turbulence Intensity

Wind tunnels are an excellent way to create a controlled environment for testing aerodynamic principles. However, some authors have criticized the results of transducer shadowing and angle of attack studies conducted in wind tunnels as the airflow can be nearly laminar (Högström & Smedman, 2004; Nakai & Shimoyama, 2012). Laminar flow does not represent the natural flow conditions of

turbulent winds and may result in skewed data or calibrations. The turbulence intensity inside the wind tunnel used in this research was calculated to be 4.09% for all three test speeds. This level of turbulence is above what is normally considered laminar, but also lower than turbulence recorded in simple flat environments like deserts or grassland (Zhang et al., 2000). As a result, airflow in the wind tunnel was consistent but also somewhat representative of natural turbulence.

4.3. TSM Wind Speed

There are two sources of error commonly encountered by sonic anemometers: angle of attack errors and transducer shadowing (Wilczak et al., 2001; Frank et al., 2015). Angle of attack errors are caused by sonic path cross-contamination when the sonic anemometer is not aligned with the mean streamline airflow. For example, this can occur when the sensor is not parallel to the surrounding terrain, in areas with significant turbulence, or mounted on an unstable drone. Transducer shadowing occurs when any structural component of the sensor obstructs or interferes with the airflow before it can be measured. Both sources of error are likely to be encountered by a sonic fixed to a multirotor drone. The two sources of error were evaluated in a carefully controlled aerodynamic environment in a wind tunnel by progressively changing the yaw rotation and pitch angle to simulate different flight conditions of an airborne drone. Tests that were completed with no angle of attack ($\theta = 0°$) replicate the aerodynamic conditions of a drone hovering in place. Test runs conducted with negative pitch angles simulate two aerodynamic environments. These tests are representative of a drone moving forward into the wind or a drone resisting drag caused by a headwind while hovering. Alternatively, test runs with positive pitch angles simulate a drone decelerating.

Yaw rotation and pitch angle were both identified as important factors in the accuracy of wind speed observations from the TSM. Interestingly, the combination of both variables attributed to mitigating or intensifying wind speed error. For example, wind speed errors caused by transducer

shadowing could be mitigated by rotating the sensor out of alignment with the wind direction. On the other hand, the wind speed error increased with steeper positive pitch angles.

Previous testing has noted that sonic anemometers can systematically underestimate wind speeds when the mean wind direction is in line with one of the instrument's support struts or transducers (Wieser et al., 2001). Wieser et al. (2001) tested several orthogonal and non-orthogonal anemometers and recorded wind speed underestimates of up to 18% when the airflow is obstructed by the anemometer's structure. Similarly, the TSM systematically underestimated the wind speed when the North support strut and lower transducer were aligned with the wind direction inside the wind tunnel ($\psi = 0°$, $\theta = 0°$) (Figure 3.8). These results indicate wind speed observations collected by a hovering drone equipped with a TSM would likely be underestimated if the wind direction was aligned with the North transducer and support strut. The wind direction could also be aligned with the North transducer and strut if the drone's ground speed is much larger than the wind speed. In this case, the apparent wind vector begins to shift and align with the drone's heading. As noted in this research and Wieser et al. (2001), the shadowing effect caused by structural interference is mitigated when airflow has an unobstructed pathway through the sensor (Figure 4.1). Generally, the most accurate wind speeds recorded by the TSM occurred halfway through the tested yaw rotations ($\psi = 40°$, $50°$).

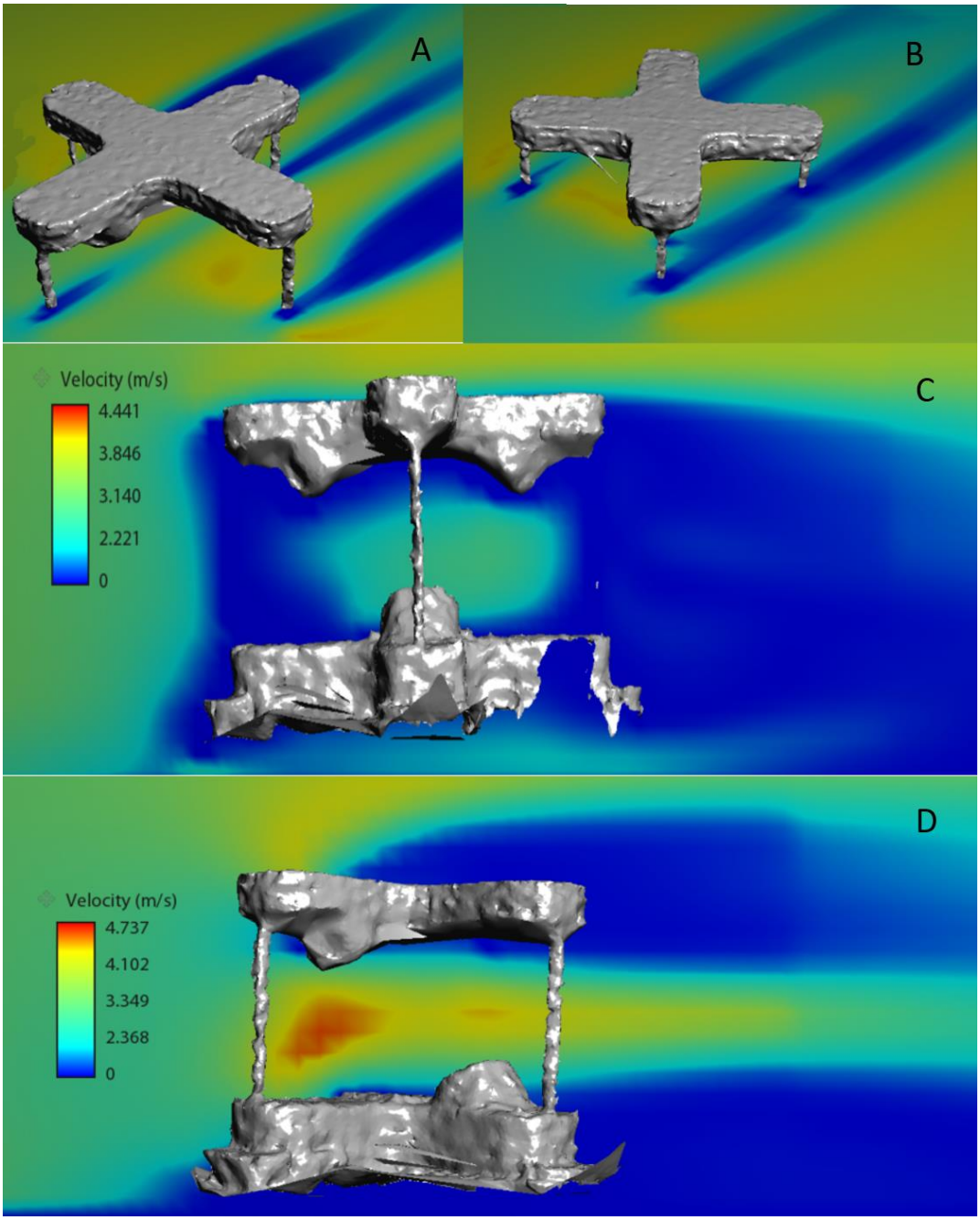

Figure 4.1: *Comparison of the TSM's aerodynamic profile using a CFD simulation (Autodesk CFD). The simulation illustrates the different aerodynamic disturbances caused by the support strut and the combination of the support strut with the transducer.* ***A)*** *TSM North strut and transducer aligned with*

mean wind direction (ψ = 0°). ***B)*** *TSM nose rotated 45° (ψ = 45°)* ***C)*** *Side view of ψ = 0°.* ***D)*** *Side view of ψ = 45°.*

Other research on transducer shadowing has documented error that has a sinusoidal shape where the maximum error is recorded near the support structures and transducers (Nakai et al., 2014; Huq et al., 2017). However, the results of this research do not follow the same trend (Figure 3.8 & Figure 3.9). Contrary to the results documented in those analyses, the TSM error was low when the transducer on the lower section of the sensor and support strut was aligned with the wind direction (ψ ≈ 90°). This may be caused by the TSM's design and transducer layout. More common 3D sonic anemometers like the Campbell Scientific CSAT3 used by Nakai et al. (2014) and Huq et al. (2017) have 3 transducer pairs offset from each other by 120°. The TSM differs from this layout as the TSM only has two transducer pairs offset by 90°. Additionally, unlike the CSAT3, the TSM design situates both transducers in a pair on the same plane so the sonic path bounces off the stipple pattern on the top and bottom section (Figure 2.1). This aligns the bottom transducer pair along the North-South axis and the top transducer pair perpendicular to the other. This design means the shape of the leading edge of the TSM is different if the wind direction is in line with the lower or upper transducer pair. The simulation in Figure 4.2 illustrates the change in the aerodynamic profile when the TSM North strut and lower transducer is in line with the wind direction and when the sensor is rotated 90° so the West strut and upper transducer is aligned with the wind direction.

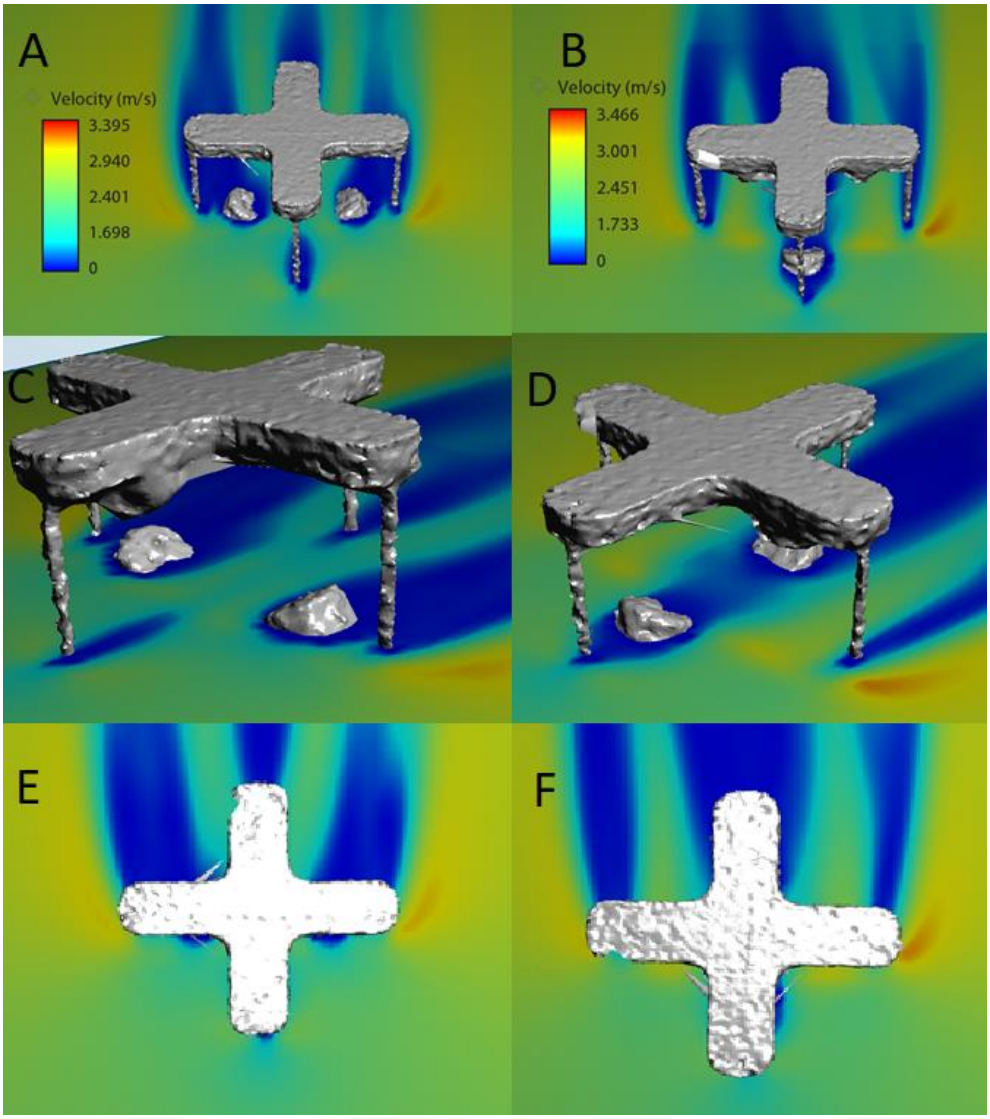

Figure 4.2: *Comparison of the TSM's aerodynamic profile with no angle of attack. The simulation illustrates the different aerodynamic disturbances caused by the support strut and the combination of the support strut with the transducer.* ***A)*** *TSM rotated to ψ =90° where the West strut is the leading edge.* ***B)*** *TSM in line with mean wind direction where the North strut is the leading edge (ψ = 0°.* ***C)*** *Side view of ψ = 90°.* ***D)*** *Side view of ψ = 0°.* ***E)*** *Top-down view of ψ = 90°.* ***F)*** *Top-down view of ψ = 0°.*

Wind speed errors relating to transducer shadowing are likely to occur if a multirotor drone equipped with a TSM is flying or hovering while aligned with the wind direction or the drone has a ground speed greater than the wind speed. Another situation that could result in severe transducer shadowing may occur when the drone reduces its groundspeed while in a headwind. When a multirotor drone decelerates, it pitches backward ($\theta > 0°$) to overcome the forward thrust vector (Figure 1.6). The TSM's specifications recommend the sensor should only be used when the pitch angle between the streamline flow and the sensor is less than ±15°. However, modern multirotor drones like the M100 can reach steep angles of attack up to 30° during aggressive maneuvers.

When a drone equipped with a TSM decelerates, the sensor is pitched backward causing the leading edge of the sensor to shadow the incoming airflow and interfere with the wind speed accuracy (Figure 4.3A). Positive angles of attack ($\theta > 0°$) that would be encountered during deceleration maneuvers would result in severely underestimated wind speeds. The largest underestimates were mostly confined to steep positive angles where the TSM transducer and support strut also interfered with the airflow. In the event a drone equipped with a TSM was aggressively decelerating while in a direct headwind, the estimated wind speed could be 60% below the true wind speed based on pitch alone (Figure 3.8). However, the shadowing effect could be mitigated in situations where a drone is not flying directly into a headwind. At steep positive angles of attack, the wind speed estimate improved when the TSM's transducer and support strut were rotated out of alignment with the wind direction. This ensures the airflow had an unobstructed pathway through the sensor (Figure 4.3B). Generally, steeper positive angles of attack required a larger yaw rotation to overcome the shadowing effect. If the TSM was fixed to a multirotor drone like the M100, the wind speed accuracy could be maintained during deceleration maneuvers and in headwinds if the sensor was rotated 45° relative to the drone's heading.

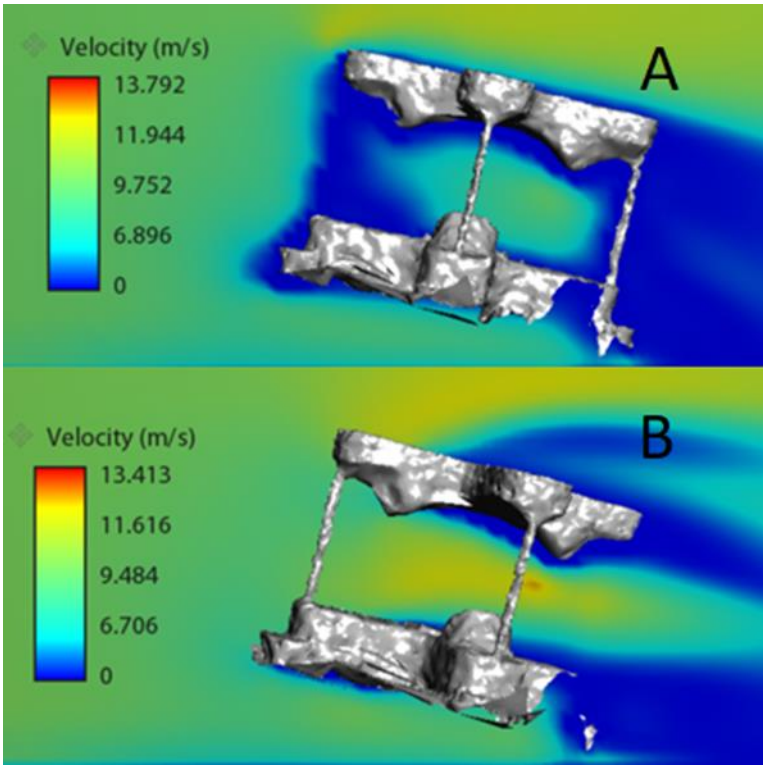

Figure 4.3: *CFD simulation of the TSM in positive angles of attack.* ***A)*** *TSM nose aligned with mean wind direction causing severe transducer shadowing (θ = 20°, ψ = 0°).* ***B)*** *TSM nose not aligned with mean wind direction (θ = 20°, ψ ≈30°).*

The final scenario that was simulated in the wind tunnel recreated the conditions encountered by a multirotor drone when accelerating or compensating for a headwind while hovering. In this case, the drone overcomes the drag force by tilting forward to produce forward thrust ($\theta < 0°$). Interestingly, the wind speed estimate collected during test runs with negative pitch angles ($\theta < 0°$) were more accurate than in positive pitch angles ($\theta > 0°$). The underestimated wind speeds recorded in tests with angles of attack equal to or greater than 0° and aligned with the wind direction ($\psi = 0°$, $\theta \geq 0°$) were not reciprocated in negative angles of attack. Similarly, the underestimated wind speeds recorded at steep positive angles of attack and small yaw rotations were not present in negative pitch angles. These results indicate small negative angles of attack could be beneficial to the wind speed accuracy as the shadowing effect was mitigated. However, tests with negative pitch angles were far more likely

to have overestimated wind speeds. Most of the overestimated wind speeds occurred during tests with negative angles of attack. Instead of shadowing the transducers, negative angles attack appeared to channel the airflow in a ramp-like effect causing overestimated wind speeds. Rotating the TSM by 45° does not appear to be as beneficial for situations where the anemometer is tilted forward. However, the rotation would not hinder data collection in negative pitch angles.

4.4. TSM Wind Direction

Transducer shadowing impacts a sonic anemometer's wind direction similar to wind speed. Previous research has noted a decrease in wind direction accuracy from sonic anemometers caused by structural interference (Wieser et al., 2001). In simulated drone conditions, yaw rotation and pitch angle were both identified as important factors that impacted the accuracy of the TSM's wind direction observations. The simulation in Figure 4.4 illustrates how the TSM's structure disrupts the airflow's path and changes the wind direction. Tests that aligned the TSM structure with the sensor systematically interfered with the airflow and caused severe deflections. Broadly speaking, the accuracy of the TSM's wind direction estimates can be split into three clusters based on the pitch angle and yaw rotation.

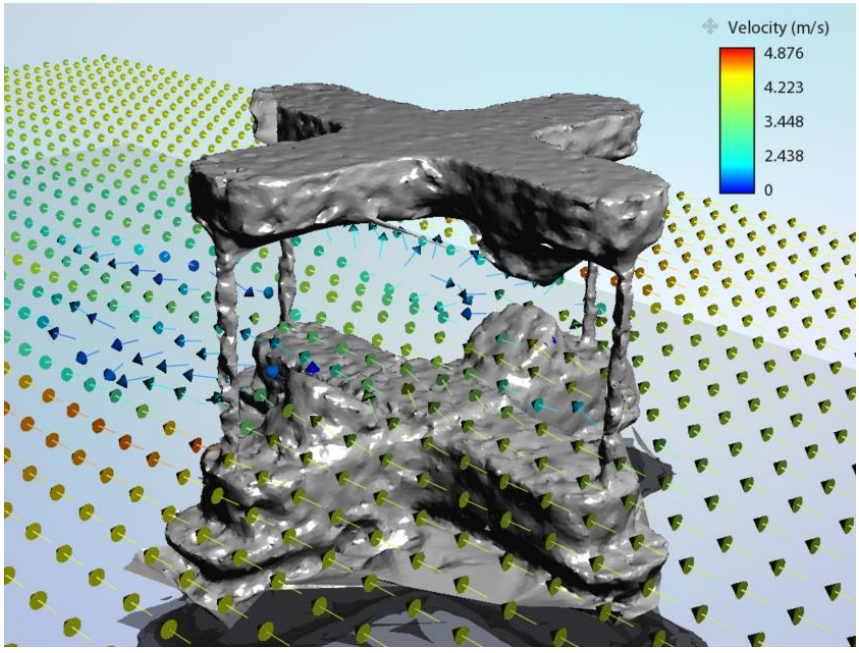

Figure 4.4: *CFD simulation of the TSM's structure interfering with wind direction. Vector arrows not pointing towards the upper left corner indicate structural interference is caused.*

The first and most accurate cluster was recorded during tests with low angles of attack and with the TSM rotated between the transducers ($\psi \approx 45°$, $\theta \leq \pm 10°$). Wind directions samples were the most accurate while the TSM was rotated so incoming airflow has a clear and direct path through the sensor. These results are similar to trends noted in the wind speed. Small angles of attack do not appear to severely impact the wind direction estimate. This scenario simulates the angles of attack that would be encountered by a multirotor drone hovering in light winds. As previously mentioned, if the TSM was mounted on a multirotor drone rotating the sensor by 45° from the front of the drone would mitigate potential transducer shadowing caused by the instrument's structure in headwinds.

The other two clusters occurred at opposite ends of the tested orientations and had opposite signs. Similar to the wind speed estimate, larger errors were recorded in tests with steep positive angles of attack and low yaw rotation ($\psi < 10°$, $\theta > 10°$). However, unlike the wind speed estimate, large overestimates were recorded in tests with steep negative angles of attack and high yaw rotation

($\psi > 80°$, $\theta < -10°$). This sinusoidal pattern of high errors occurring when incoming airflow is shadowed by the sensor's structure has been noted in other research (Nakai et al., 2014; Huq et al., 2017). Both clusters were primarily contained within 20° of the closest transducer and support strut. As previously mentioned, steep positive angles of attack are encountered by a drone during deceleration maneuvers, whereas steep negative angles of attack can occur in strong headwinds or when accelerating. The severity of errors related to transducer shadowing recorded by a TSM mounted on a multirotor drone during steep angles of attack could be mitigated by rotating the sensor 45° from the front of the drone. In steep angles of attack, the wind direction estimate was more accurate when the TSM was rotated halfway between the transducers ($\psi \approx 45°$).

In the TSM's case, the sign of the wind direction estimate indicated an interesting pattern of deflection was present. When the TSM's upper transducer and support strut were aligned with the mean wind direction ($\psi = 0°$) the airflow was consistently deflected to the left around the obstacle. Whereas, when the TSM's lower transducer and support strut were aligned with the mean wind direction ($\psi = 90°$) the airflow was deflected to the right. This pattern may be caused by the TSM's novel transducer pair layout (Figure 2.1).

4.5. Rotor Wash and Drone Induced Wind Speed

The rotor wash analysis conducted in this research attempted to locate positions above the M100 that would situate the TSM in an area where the wind speed and wind direction were not significantly distorted. A total of 77 tests were completed at different positions above the M100 rotors. More tests could have been completed further from the rotors vertically and horizontally, however positioning an anemometer in these locations could create new sources of error. For example, adding structural elements to a multirotor changes the aircraft's center of gravity. A long support shaft could remove the anemometer from the rotor wash but drastically change the stability and flight performance of the aircraft as the length of the shaft has an exponential impact on shifting the center

of gravity. Similarly, if the shaft is not properly secured vibrations generated by the drone can travel through the shaft and create interference. The severity of these vibrations is also related to the length of the beam used. Lastly, the length of the beam is proportional to the induced wind speed generated during attitude adjustments. A small change in the drone's angle of attack shifts the anemometer along an arc at the end of the shaft. Multirotor drones like the M100 have a maximum pitch velocity of 300° per second, and a maximum yaw velocity of 150°. Tip speed as a function of rotation and shaft length is shown in Figure 4.5. Ultimately, this results in a problem akin to extracting the wind vector from a moving platform using the wind triangle (Figure 4.3). Positioning a sonic anemometer on a long mast could mitigate errors related to the drone's rotor wash, however, this could introduce new sources of error that would need to be investigated.

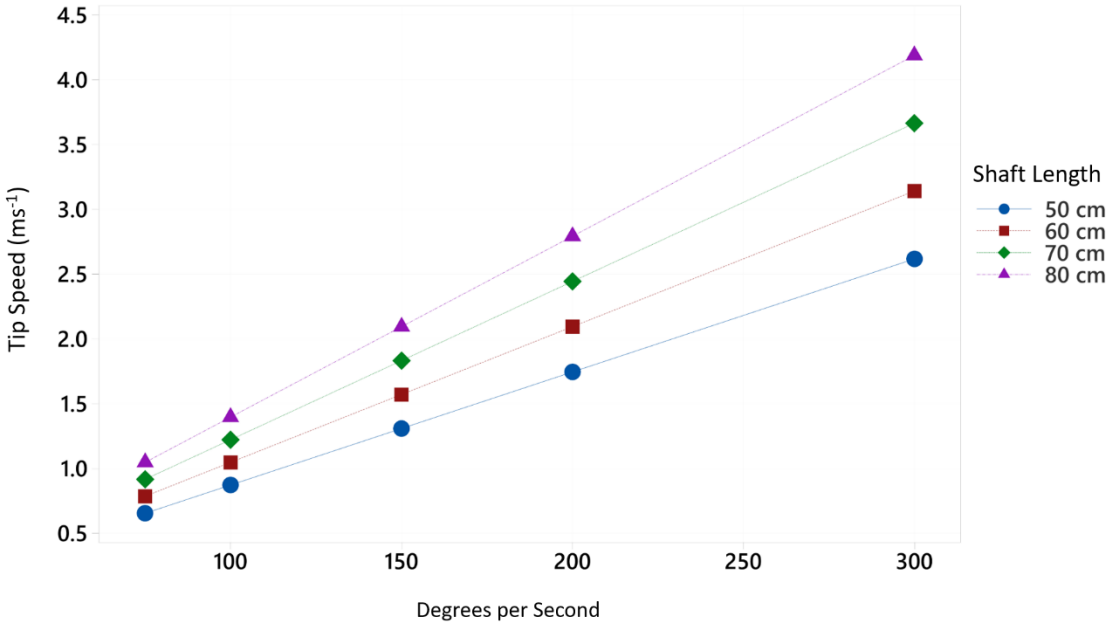

Figure 4.5: *Wind speed generated as a function of rotation speed and shaft length.*

As previously noted, during the simulated hover test the M100 was not able to maintain the necessary rotor RPM to hover during the testing. After the M100 was fixed to the mast and commanded to hover several flight warnings appeared in the flight application and the M100

attempted to safely land. If the rotor RPM was fixed at a threshold below the minimum hover RPM, the rotors remained at a consistent speed. It is estimated the test was conducted at 80% of the true hover RPM.

The rotor wash analysis conducted in this research followed a procedure similar to Alvarado et al., (2017). In this research, some adaptations were made to improve the resolution and quality of observations. As discussed in section 2.2.2, inertial anemometers are commonly used for long-term observations. Alvarado et al., (2017) mounted a hand-held Kestrel 2500 to a separately adjustable mast so that the sensor could be moved. The Kestrel 2500 is an inertial-based anemometer similar to the Cup anemometers discussed in section 2.2.2. However, the Kestrel measures the rotation of an array of fins, known as an impeller, around a horizontal axis to estimate wind speed. Several sources of error that impact inertial anemometers are often encountered during this application. One source of error that impacts rotational anemometers is the inertia stored in the rotating impeller. Inertial anemometers tend to over or under-estimate wind speeds when the airspeed is rapidly changed (Wyngaard, 1981). Smith et al. (2016) noted there are stark boundaries between the air that is stagnant (not impacted) and turbulent (impacted) above the rotors of a drone. Additionally, at low wind speeds, inertial anemometers are impacted by unpredictable changes in friction on the internal bearing. This results in a non-linear, less predictable relationship between wind speed and rotation (Kristensen, 1999). According to the Kestrel user manual, the instrument used by Alvarado et al. (2017) is not recommended for measuring wind speeds below 0.4 m s^{-1} (Kestrel Instruments, 2020). For these reasons, the TSM was used to avoid the potential sources of error encountered by inertial anemometers.

The contour plot in Figure 3.10 illustrates significantly disrupted airflow near the rotors of the DJI M100. Rotor wash contamination decreases as the measurements were taken further away from the rotors. Interestingly, there are several pockets of turbulent airflow spaced out by 10 to 15 cm

directly above the center of the M100. These pockets are referred to as ingested vortices and are likely caused by the interaction between counter-rotating vertical flows above each rotor (Yoon et al., 2016). Similar to how the impact of transducer shadowing will change depending on the design of the sonic anemometer, so too will the shape of the rotor flow interference generated by different drones. However, the results from the M100 rotor wash analysis agree with testing conducted on similar-sized drones in the literature (Alvarado et al., 2017; Hollenbeck et al., 2018). Alvarado et al. (2017) found that 45 cm above the center of the 3DR IRIS+ quadcopter the impact of rotor wash was not significant, whereas Hollenbeck et al. (2018) reported the same at 39 cm with a Foxtech Hover1 quadcopter.

Hollenbeck et al. (2018) conducted the rotor wash analysis in a low-cost wind tunnel (LCWT) and found the disturbances generated by a drone's rotors increases as the throttle speed is increased. However, Smith et al. (2016) noted that above airspeeds of 2 m s^{-1} the impact of rotor wash contamination above the drone diminishes. The impact of rotor wash contamination changes depending on how the drone is oriented relative to the mean wind direction. For example, the impact of rotor wash contamination is increased for quad-copters if the drone is rotated 45° from the mean wind direction (Bruschi et al., 2016). This results in the typical quad-copter design aligning one of the rotors with the mean wind direction. Similarly, the shape of the wash generated by the rotors changes depending on the aircraft's attitude. Simulated flight tests conducted in LCWT show that forward tilt in relation to the wind direction reduces the impact of rotor wash contamination, whereas, backward tilt increases the effect (Hollenbeck et al., 2019).

4.6. Apparent Wind Direction caused by Rotor Wake and Drone Movement

Most of the challenges that apply to collecting accurate and precise wind speed data from a multirotor drone also apply to wind direction observations. As previously mentioned, positioning an anemometer above a multirotor drone is a complex balance of operations. Shifting the sensor further from the rotors may mitigate the rotor contamination on the anemometer but introduce new untested sources of error such as excessive vibration. Another potential source of error relates to the induced wind speed caused by the drone's attitude adjustment. Maneuvers that adjust the drone's angle of attack and yaw can change the apparent wind speed recorded by the anemometer. This change in the wind speed causes a shift in the apparent wind direction along the circumference of rotation. The apparent wind direction would shift according to a process similar to the wind triangle where a moving object feels an apparent wind speed different from the true wind speed (Figure 1.3).

The wind direction shift above the drone appears to be organized by the sample's lateral location in relation to the rotors. Wind direction samples taken over the front of the drone were close to the reference wind direction. More specifically, samples taken at least 20 cm in front of the M100 center were in close agreement with the reference. Whereas samples taken over the back of the drone indicated the airflow was coming from the opposite direction compared to the reference.

The boundary between wind direction samples that were aligned with the reference and samples that were disturbed occurred approximately 20 cm in front of the M100 center. The same boundary is more clearly illustrated in the wind direction standard deviation contour plot (Figure 3.13). Wind direction standard deviation increases at the same horizontal location for samples taken up to 30 cm above the rotors. For samples taken 40 cm or higher, the increase in standard deviation generally occurred closer to the center of the M100. Interestingly, at low heights above the rotors, the boundary between undisturbed and disturbed airflow appears to occur approximately above the center of the M100 rotors. These results indicate there is less rotor-induced wind direction interference on the

headwind side of a multirotor drone when the airflow travels between the two front rotors. When airflow passed between the front rotors and began to interact with the rear rotors samples were generally more turbulent. The airflow on the headwind side of the drone appears to be most consistent with the reference which means it would be advantageous to bias the position of an anemometer on an M100 towards the nose of the drone and at least 30 cm above the rotors.

Because the conditions in the test facility remained consistent throughout testing these results only apply to similar situations. The wind direction flowed from the nose of the drone to the rear between the rotors. If the airflow's path instead was ±45° from the nose of the drone the results would likely be drastically different. In this case, the leading rotor would cause a different disturbance pattern similar to the change in wind speed noted in previous research (Bruschi et al., 2016). Additionally, several other scenarios that were not tested in this research could have severe implications on wind direction observations. These scenarios include different ambient wind speeds, throttle conditions, and angles of attack. As mentioned in the wind speed section of the rotor wash analysis, increased ambient wind speed can have a beneficial impact and mitigate rotor wash contamination (Smith et al., 2016), whereas increasing the rotor throttle can cause more severe turbulence to occur above the drone (Hollenbeck et al., 2018). Lastly, negative angles of attack appear to provide a similar benefit (Hollenbeck et al., 2018)(Smith et al., 2016).

4.7. Summary and Recommendations for Drone Based Sonic Anemometry

The TSM is an example of the first generation of sonic anemometers that are small and light enough to be compatible with small modern multirotor drones. However, this research has identified and analyzed several sources of error that may impact the accuracy of observations from a sonic anemometer mounted on a multirotor drone. This includes errors relating specifically to the sensor and the drone. These errors are not exclusive to the TSM and M100 platforms and are shared by all drones equipped with sonic anemometers. Although, the impact of these errors will change with the design of

the anemometer and drone. Drones equipped with sonic anemometers may become a viable method of attaining in-situ meteorological and atmospheric observations. For example, this method could be deployed to provide vertical wind profile observations or to collect data in areas that are unsafe for humans to access (Astuti et al., 2008; Caltabiano et al., 2006). However, several parameters and conditions need to be met or known to ensure data collection is robust enough to provide accurate and precise observations. The following points summarize notable findings and related recommendations for drone-based sonic anemometry that were identified during this research:

a. A sonic anemometer's observational accuracy of wind direction and wind speed is related to the angle of attack and incoming wind direction. This relationship can be beneficially exploited as small angles of attack mitigate the impact of transducer shadowing in some scenarios

b. A sonic anemometer's structural design has a significant influence on how the airflow moves through or deflects around the sensor.

c. Compared to conventional sonic anemometers, small sonic anemometers like the TSM have larger relative obstructions from struts and transducers.

d. Before a sonic anemometer is deployed on a drone, the sensor should be calibrated to integrate potential angle of attack or transducer shadowing errors.

e. Mounting a sonic anemometer to a drone requires careful consideration to mitigate interference from the rotors, vibrations, induced wind speed, and wind direction. Additionally, the structural components needed to facilitate the anemometer must not interfere with the flight dynamics of the drone.

f. The shape and intensity of interference generated by a drone's rotors is related to the angle of attack, incoming wind direction, and rotor speed.

g. Similar to the finding noted in “a”, this relationship between rotor flow interference, angle of attack, and wind direction can be beneficially exploited as small angles of attack or headwinds can mitigate the interference above the drone.

h. Unstable or gusty wind environments may create challenging flight conditions and result in a highly unstable drone. These conditions inhibit drone-based sonic anemometry as rapid changes in the drone's attitude adds complexity and uncertainty when calculating wind speed and direction.

i. Sampling should be avoided during deceleration maneuvers as the intensity of rotor wash interference above the drone may increase.

Chapter 5: Conclusion

5.1. Miniaturized Sonic Anemometers for Drone-based Applications

The first generation of small sonic anemometers, such as the TSM, are adapting and expanding approaches used to collect atmospheric data. In addition, modern drones are revolutionizing the way in-situ data can be collected safely. The combination of a miniaturized sonic anemometer and small drones have the potential to develop into a powerful observation method for many applications. However, the results from this research have identified, analyzed, and discussed several sources of error that need to be addressed before this combination of technologies is used to collect data in the field. All drones equipped with sonic anemometers will encounter the errors discussed in this research, but the impact will change depending on the sensor and drone design. A major feature of the TSM is the small size of the sensor. However, the transducers and support struts on the TSM are similar in size to larger sonic anemometers despite the smaller sampling volume. This results in the TSM structure blocking or interfering with a larger portion of the air flowing through the sampling volume.

The angle of attack and transducer shadowing tests conducted in a wind tunnel simulated the aerodynamic environment and instability of a drone in flight. The TSM wind speed and direction estimate accuracy changes significantly depending on the sensor's pitch angle and yaw rotation relative to the wind direction. As the sensor is rotated and tilted, the aerodynamic profile of the sensor changes and introduces or removes obstacles that cause the airflow to be disturbed. Generally, accurate and consistent results occurred when the TSM was rotated so the sensors transducers and support struts were not aligned with the mean wind direction. Even in low angles of attack, this configuration gives incoming airflow a direct unobstructed path through the sensor. This results in wind direction and wind speed observations that were close to the reference values.

A rotor wash analysis identified several areas above the M100 as suitable locations for mounting a sonic anemometer. The locations identified did not incur a significant amount of disturbance generated by the drone's rotors while in a simulated hover. Because the test was conducted with the rotors below the true hover RPM the areas of interference are expected to be larger than they are presented here. The region directly above the body of the M100 displays intermittent ingested rotor wash vortices. These pockets of turbulent air could result in poor observational accuracy.

Positioning a sonic anemometer on a multirotor drone requires a careful balance of operations. As incoming airflow interacts with the drone's rotors it becomes turbulent and thus differs from the true conditions. On one hand, using a long mast could remove the sensor from rotor wash interference, in contrast, this could cause flight problems and generate additional sources of error. The results of this research indicate an ideal location for a sonic anemometer is around 50 cm above the drone's rotors and above and in front of the leading rotors. Lastly, the process of measuring rotor wash interference should be repeated with the mounting structures in place as they may cause new interference patterns to be generated.

The shape and impact of rotor wash disturbance is known to change depending on the drone's attitude in relation to the mean wind direction (Smith et al., 2016). Other research has discovered that the impact of rotor wash diminishes as airspeed increases (Hollenbeck et al., 2018). Several flight conditions could be beneficially exploited or avoided to mitigate potential rotor wash contamination. For example, data collection should be avoided during deceleration maneuvers. A decelerating drone causes positive angles of attack that not only cause errors related to transducer shadowing but are also known to increase rotor-induced interference above the drone's body. Whereas increased airspeed and negative angles of attack could be ideal for quality data collection. Negative angles of attack may reduce rotor wash contamination while not interfering with TSM accuracy.

Drones equipped with sonic anemometers can be a valuable tool for atmospheric, meteorological, or emission detection applications. However, there is a complex balance of operations that will impact the reliability of the observations. The TSM is small and light enough to be fixed to a multirotor drone, but the instability of the platform and turbulence it generates may interfere with the wind speed and direction estimates. Optimal wind speed and direction observations collected from multirotor drones equipped with sonic anemometers requires several conditions to be met. Firstly, the sensor needs to be mounted in a location above the body of the drone that does not interfere with fight conditions. Additionally, the sensor needs to be positioned so the rotor wash generated by the drone does not interfere with the airflow. Controlled aerodynamic testing of the TSM identified a strong relationship between the sensor orientation to the mean wind direction and the observational accuracy. Specifically, rotating the TSM so the structural components of the sensor are not in line with the mean wind direction creates an obstacle-free pathway for the airflow. Rotating the sensor to create a direct pathway for the airflow also enables accurate observations at small angles of attack or tilts. Small angles of attack have also been shown to be beneficial as the impact of rotor wash above the drone is decreased (Smith et al., 2016). A drone in an orientation with an angle of attack implies the aircraft is overcoming drag caused by increased airspeed which is generated by the drone's movement or wind. Increased airspeed also attributes to decreasing the overall impact of rotor wash. Lastly, the TSM wind speed estimate accuracy increases with airspeed.

5.2. Future Work

The angle of attack and transducer shadowing tests conducted in this research only investigated 90° of yaw rotation. Due to the symmetry of the sensor, it is assumed that this relationship repeats for the remaining 270° similar to the results found in other research (Wieser et al., 2001). This testing could be repeated to provide a full 360° analysis of transducer shadowing and angle of attack errors. The aerodynamic modeling used in this research served as a method of

visualizing the complex aerodynamic principles at play. The modeling used relatively simple parameters to illustrate the airflow interactions, however, more complex modeling could improve the observations and results.

Because the rotor wash test was not conducted while the rotors were at the RPM necessary to hover, the interference likely impacts a larger area around the body than presented in this research. Before the M100 can be used for atmospheric or meteorological research a more realistic hover test to assess the turbulence generated by the rotors needs to be completed first. More rotor wash tests conducted with lateral positions or positions in front of the drone could identify ideal anemometer locations. Similarly, testing could be completed with the intent of mounting two or more sonic anemometers. Additionally, several parameters including aircraft attitude and the influence of ambient airflow were not investigated but have been identified as significant variables in other research (Hollenbeck et al., 2018, 2019; Smith et al., 2016). The impact of these variables could be examined in a controlled aerodynamic environment like the wind tunnel used in this research.

This research targeted several known sources of error and investigated them individually in controlled environments. Other studies have shown that many of the sources of error discussed in this research are have a strong relationship with each other (Sam Prudden & Mohamed, 2016; Smith et al., 2016; Wieser et al., 2001). The impact of some sources of error discussed in this research may be amplified or diminished by others. The results of this research demonstrate that in certain scenarios it should be possible for a drone equipped with a sonic anemometer to provide accurate wind speed and direction observations. However, flight tests are required to fully examine the limitations and potential of this method.

References

3D Flow. (2020). 3DF Zephyr Lite Manual.

Aich, S., Ahuja, C., Gupta, T., & Arulmozhivarman, P. (2014). Analysis of Ground Effect on Multi-Rotors. 2014 *International Conference on Electronics, Communication and Computational Engineering (*ICECCE*)*, 236–241. https://doi.org/10.1109/ICECCE.2014.7086619

Alvarado, M., Gonzalez, F., Erskine, P., Cliff, D., & Heuff, D. (2017). A methodology to monitor airborne PM10 dust particles using a small unmanned aerial vehicle. *Sensors* (Switzerland), 17(2). https://doi.org/10.3390/s17020343

Anemoment, L. (2019). World's Smallest & Lightest 3D Ultrasonic Anemometer TriSonica TM Mini Wind & Weather Sensor. https://www.anemoment.com/

Arain, B., & Kendoul, F. (2014). Real-time wind speed estimation and compensation for improved flight. IEEE *Transactions on Aerospace and Electronic Systems*, 50(2), 1599–1606. https://doi.org/10.1109/TAES.2014.120236

Ashcroft. (2009). Ashcroft DP sensor Maintenance Sheet (Issue 238).

Astuti, G., Longo, D., Melita, C. D., Muscato, G., & Orlando, A. (2008). HIL tuning of UAV for exploration of risky environments. *International Journal of Advanced Robotic Systems*, 5(4), 419–424. https://doi.org/10.5772/6227

Bartholmai, M., & Neumann, P. (2010). Micro-Drone for Gas Measurement in Hazardous Scenarios via Remote Sensing 2 Development of a Mobile Measure- ment System. *Selected Topic in Power Systems and Remote Sensing*, 149–152.

Bonin, T. A., Chilson, P. B., Zielke, B. S., Klein, P. M., & Leeman, J. R. (2013). Comparison and application of wind retrieval algorithms for small unmanned aerial systems. *Geoscientific Instrumentation Methods and Data Systems*, 177–187. https://doi.org/10.5194/gi-2-177-2013

Brosy, C., Krampf, K., Zeeman, M., Junkermann, W., Emeis, S., Krampf, K., Kunstmann, H., Brosy, C., Zeeman, M., Wolf, B., & Schäfer, K. (2017). Simultaneous multicopter-based air sampling and sensing of meteorological variables. *Atmospheric Measurement Techniques*, 10(8), 2773–2784. https://doi.org/10.5194/amt-10-2773-2017

Bruschi, P., Piotto, M., Dell'Agnello, F., Ware, J., & Roy, N. (2016). Wind Speed and Direction Detection by Means of Solid-state Anemometers Embedded on Small Quadcopters. *Procedia Engineering*, 168, 802–805. https://doi.org/10.1016/j.proeng.2016.11.274

Caltabiano, D., Muscato, G., Orlando, A., Federico, C., Giudice, G., & Guerrieri, S. (2006). Architecture of a UAV for volcanic gas sampling. 739–744. https://doi.org/10.1109/etfa.2005.1612599

Campbell Scientific. (2017). CSAT3 Three Dimensional Sonic Anemometer Manual.

Cho, A., Kim, J., Lee, S., & Kee, C. (2011). Wind Estimation and Airspeed Calibration using a UAV with a Single-Antenna GPS Receiver and Pitot Tube. *IEEE Transactions on Aerospace and Electronic Systems*, 47(1), 109–117. https://doi.org/10.1109/TAES.2011.5705663

Diego, S., & Jolla, L. (2016). The Influence of Wind Direction on Campbell Scientific CSAT3 and Gill R3-50 Sonic Anemometer Measurements. 2477–2497. https://doi.org/10.1175/JTECH-D-16-0055.1

Donnell, G. W., Feight, J., Lannan, N., & Jacob, J. (2018). Wind Characterization Using sUAS. 1–25. https://doi.org/10.2514/6.2018-2986

Elston, J., Argrow, B., Stachura, M., Weibel, D., Lawrence, D., & Pope, D. (2015). Overview of Small Fixed-Wing Unmanned Aircraft for Meteorological Sampling. *Journal of Atmospheric and Oceanic Technology*, 97–115. https://doi.org/10.1175/JTECH-D-13-00236.1

Frank, J. M., Massman, W., Swiatek, E., Zimmerman, H., & Ewers, B. (2015). All Sonic Anemometers Need to Correct for Transducer and Structural Shadowing in Their Velocity Measurements. *Journal of Atmospheric and Oceanic Technology*, 149–167. https://doi.org/10.1175/JTECH-D-15-0171.1

Gash, J. H. C., & Dolman, A. J. (2003). Sonic anemometer (co)sine response and flux measurement I. The potential for (co)sine error to affect sonic anemometer-based flux measurements. *Agricultural and Forest Meteorology*, 119(3–4), 195–207. https://doi.org/10.1016/S0168-1923(03)00137-0

Ghanadi, F., Emes, M., Yu, J., & Arjomandi, M. (2017). Investigation of the atmospheric boundary layer characteristics on gust factor for the calculation of wind load Investigation of the Atmospheric Boundary Layer Characteristics on Gust Factor for the Calculation of Wind Load. *AIP Conference Proceedings* 1850, 130002(June). https://doi.org/10.1063/1.4984496

Giebel, G., Schmidt, P., Uwe, J., :a Cour-Harbo, A., Reuder, J., Mayer, S., van der Kroonenberg, A., & Molgaard, J. (2012). Autonomous Aerial Sensors for Wind Power Meteorology - A Pre-Project Risø-R-Report. Danmarks Tekniske Universitet, Risø Nationallaboratoriet for Bæredygtig Energi. Denmark. Forskningscenter Risoe. Risoe-R, No. 1798(EN).

Gill. (2019). WindMaster 3-Axis Ultrasonic Anemometer Manual.

Golston, L. M., Aubut, N. F., Frish, M. B., Yang, S., Talbot, R. W., Gretencord, C., McSpiritt, J., & Zondlo, M. A. (2018). Natural gas fugitive leak detection using an unmanned aerial vehicle: Localization and quantification of emission rate. *Atmosphere*, 9(9). https://doi.org/10.3390/atmos9090333

González-Rocha, J., Woolsey, C. A., Sultan, C., & De Wekker, S. F. J. (2019). Sensing Wind from Quadrotor Motion. *Journal of Guidance, Control, and Dynamics*, 42(4), 836–852. https://doi.org/10.2514/1.g003542

Grelle, A., & Lindroth, A. (1994). Flow Distortion by a Solent SOnic Anemometer: Wind Tunnel Calibration and Its Assessment for Flux Measurements over Forest and Field. *American Meteorlogical Society*.

Harper, B. A., Kepert, J. D., & Ginger, J. D. (2010). Guidelines for Converting Between Various Wind Averaging Periods in Tropical Cyclone Conditions.

Högström, U., & Smedman, A. S. (2004). Accuracy of sonic anemometers: Laminar wind-tunnel calibrations compared to atmospheric in situ calibrations against a reference instrument. *Boundary-Layer Meteorology*, 111(1), 33–54. https://doi.org/10.1023/B:BOUN.0000011000.05248.47

Hollenbeck, D., Nunez, G., Christensen, L. E., & Chen, Y. (2018). Wind Measurement and Estimation with Small Unmanned Aerial Systems (sUAS) Using On-Board Mini Ultrasonic Anemometers. 2018 *International Conference on Unmanned Aircraft Systems*, ICUAS 2018, 285–292. https://doi.org/10.1109/ICUAS.2018.8453418

Hollenbeck, D., Oyama, M., Garcia, A., & Chen, Y. (2019). Pitch and Roll Effects of On-board Wind Measurements Using sUAS. 2019 *International Conference on Unmanned Aircraft Systems* (ICUAS), 1249–1254. https://doi.org/10.1109/icuas.2019.8797707

Hüllmann, D., Paul, N., Kohlhoff, H., Neumann, P. P., & Lilienthal, A. J. (2018). Measuring rotor speed for wind vector estimation on multirotor aircraft. *Materials Today: Proceedings.* https://doi.org/10.1016/j.matpr.2018.08.139

Huq, S., Roo, F. De, Foken, T., & Mauder, M. (2017). Evaluation of Probe-Induced Flow Distortion of Campbell CSAT3 Sonic Anemometers by Numerical Simulation. *Boundary-Layer Meteorology*, 165(1), 9–28. https://doi.org/10.1007/s10546-017-0264-z

Kaimal, J. C., Gaynor, J. E., Zimmerman, H. A., & Zimmerman, G. A. (1990). Minimizing flow distortion errors in a sonic anemometer. *Boundary-Layer Meteorology*, 53(1–2), 103–115. https://doi.org/10.1007/BF00122466

Kestrel Instruments. (2020). Kestrel User guide.

Klopfenstein Jr, R. (1998). Air velocity and flow measurement using a Pitot tube. *ISA Transactions*, 37(4), 257–263. https://doi.org/10.1016/S0019-0578(98)00036-6

Konrad, T. G., Hill, M. L., Rowland, J. R., & Meyer, J. H. (1970). A Small, Radio-Controlled Aircraft As A Platform for Meteorlogical Sensors. *APL Technical Digest, December*, 11–19.

Kristensen, L. (1999). The perennial cup anemometer. *Wind Energy*, 2(1), 59–75. https://doi.org/10.1002/(sici)1099-1824(199901/03)2:1<59::aid-we18>3.0.co;2-r

Kristensen, Leif. (1998). Cup Anemometer Behavior in Turbulent Environments. *American Meteorlogical Society*, 1969, 5–17.

Mahony, R., Kumar, V., & Corke, P. (2012). Multirotor aerial vehicles: Modeling, estimation, and control of quadrotor. *IEEE Robotics and Automation Magazine*, 19(3), 20–32. https://doi.org/10.1109/MRA.2012.2206474

Marino, M., Fisher, A., Clothier, R., Watkins, S., Prudden, S., & Leung, C. S. (2015). An Evaluation of Multi-Rotor Unmanned Aircraft as Flying Wind Sensors. *International Journal of Micro Air Vehicles*, 7(3), 285–299. https://doi.org/10.1260/1756-8293.7.3.285

Martin, S., Bange, J., & Beyrich, F. (2011). Meteorological profiling of the lower troposphere using the research UAV " M 2 AV Carolo ." *Atmospheric Measurement Techniques*, 705–716. https://doi.org/10.5194/amt-4-705-2011

Mayer, S., Hattenberger, G., Brisset, P., Jonassen, M. O., & Reuder, J. (2012). A 'No-Flow-Sensor' Wind Estimation Algorithm for Unmanned Aerial Systems. *International Journal of Micro Air Vehicles*, 4(1), 15–29. https://doi.org/10.1260/1756-8293.4.1.15

Nakai, T., Iwata, H., Harazono, Y., & Ueyama, M. (2014). An inter-comparison between Gill and Campbell sonic anemometers. *Agricultural and Forest Meteorology*, 195–196, 123–131. https://doi.org/10.1016/j.agrformet.2014.05.005

Nakai, T., & Shimoyama, K. (2012). Ultrasonic anemometer angle of attack errors under turbulent conditions. *Agricultural and Forest Meteorology*, 162–163, 14–26. https://doi.org/10.1016/j.agrformet.2012.04.004

Nakai, T., Van Der Molen, M. K., Gash, J. H. C., & Kodama, Y. (2006). Correction of sonic anemometer angle of attack errors. *Agricultural and Forest Meteorology*, 136(1–2), 19–30. https://doi.org/10.1016/j.agrformet.2006.01.006

Nathan, B. J., Golston, L. M., Brien, A. S. O., Ross, K., Harrison, W. A., Tao, L., Lary, D. J., Johnson, D. R., Covington, A. N., Clark, N. N., & Zondlo, M. A. (2015). Near-Field Characterization of Methane Emission Variability from a Compressor Station Using a Model Aircraft. *Enviromentental Science & Technology*. https://doi.org/10.1021/acs.est.5b00705

Neumann, P. P., & Bartholmai, M. (2015). Real-time wind estimation on a micro unmanned aerial vehicle using its inertial measurement unit. *Sensors and Actuators, A: Physical*, 235, 300–310. https://doi.org/10.1016/j.sna.2015.09.036

Niedzielski, T., Skjøth, C., & Spallek, W. (2017). Are estimates of wind characteristics based on measurements with Pitot tubes and GNSS receivers mounted on consumer-grade unmanned aerial vehicles applicable in meteorological studies ? *Enviromental Monitoring and Assessment*. https://doi.org/10.1007/s10661-017-6141-x

Palomaki, P., Rose, N. T., van den Bossche, M., Sherman, T. J., & de Weller, S. F. J. (2017). Wind Estimation in the Lower Atmosphere Using Multirotor Aircraft. *American Meteorlogical Society*, 1183–1191. https://doi.org/10.1175/JTECH-D-16-0177.1

Peña, A., Dellwik, E., & Mann, J. (2019). A method to assess the accuracy of sonic anemometer measurements. *Atmospheric Measurement Techniques*, 2004, 237–252.

Prudden, S., Fisher, A., Marino, M., Mohamed, A., Watkins, S., & Wild, G. (2018). Measuring wind with Small Unmanned Aircraft Systems. *Journal of Wind Engineering and Industrial Aerodynamics*, 176(March), 197–210. https://doi.org/10.1016/j.jweia.2018.03.029

Prudden, S, Fisher, A., Mohamed, A., & Watkins, S. (2017). An Anemometer for UAS-based Atmospheric Wind Measurements. *International Journal of Micro Air Vehicles*, February, 26–28.

Prudden, Sam, & Mohamed, A. (2016). A Flying Anemometer Quadrotor : Part 1. The International *Micro Air Vehicle Conference and Competition*, October 2016.

Rautenberg, A., Graf, M. S., Wildmann, N., Platis, A., & Bange, J. (2018). Reviewing Wind Measurement Approaches for Fixed-Wing Unmanned Aircraft. *Atmosphere*, 1–24. https://doi.org/10.3390/atmos9110422

Reineman, B. D., Lenain, L., Statom, N. M., & Melville, K. K. (2013). Development and testing of instrumentation for UAV-based flux measurements within terrestrial and marine atmospheric boundary layers. *Journal of Atmospheric and Oceanic Technology*, 30(7), 1295–1319. https://doi.org/10.1175/JTECH-D-12-00176.1

Reuder, J., Brisset, P., Jonassen, M., Müller, M., & Mayer, S. (2009). The Small Unmanned Meteorological Observer SUMO: A new tool for atmospheric boundary layer research. *Meteorologische Zeitschrift*, 18(2), 141–147. https://doi.org/10.1127/0941-2948/2009/0363

Riddell, K. D. A. (2014). Design, testing and demonstration of a small unmanned aircraft system (SUAS) and payload for measuring wind speed and particulate matter in the atmospheric boundary layer. University of Lethbridge.

Schuyler, T., & Guzman, M. (2017). Unmanned Aerial Systems for Monitoring Trace Tropospheric Gases. *Atmosphere*, 8(12), 206. https://doi.org/10.3390/atmos8100206

Shepherd, I. C. (1981). A Four Hole Pressure Probe for Fluid Flow Measurements in Three Dimensions. *Journal of Fluids Engineering*, 103(4), 590. https://doi.org/10.1115/1.3241774

Shimura, T., Inoue, M., Tsujimoto, H., Sasaki, K., & Iguchi, M. (2018). Estimation of Wind Vector Profile Using a Hexarotor Unmanned Aerial Vehicle and Its Application to Meteorological Observation up to 1000 m above Surface. *Journal of Atmospheric and Oceanic Technology*, 1621–1631. https://doi.org/10.1175/JTECH-D-17-0186.1

Smith, B., John, G., Stark, B., Christensen, L. E., & Chen, Y. Q. (2016). Applicability of unmanned aerial systems for leak detection. *2016 International Conference on Unmanned Aircraft Systems*, ICUAS 2016, October 2017, 1220–1227. https://doi.org/10.1109/ICUAS.2016.7502635

Sotelino, L. G., Coster, N. D., Beirinckx, P., & Peeters, P. (2012). Intercomparison of cup anemometer and sonic anemometers on site at Uccle/Belgium. *WMO Technical Conference*, 1–7. https://www.wmo.int/pages/prog/www/IMOP/publications/IOM-109_TECO-2012/Session1/P1_08_GonzalezSotelino_intercomp_anemometers_UCCLE.pdf

Suomi, I., & Vihma, T. (2018). Wind gust measurement techniques—From traditional anemometry to new possibilities. *Sensors*, 18(4), 1–27. https://doi.org/10.3390/s18041300

van der Kroonenberg, A., Martin, T., Buschmann, M., Bange, J., & Vorsman, P. (2008). Measuring the Wind Vector Using the Autonomous Mini Aerial Vehicle M 2 AV. *Journal of Atmospheric and Oceanic Technology*, 1991, 1969–1982. https://doi.org/10.1175/2008JTECHA1114.1

Van Der Molen, M. K., Gash, J. H. C., & Elbers, J. A. (2004). Sonic anemometer (co)sine response and flux measurement: II. The effect of introducing an angle of attack dependent calibration. *Agricultural and Forest Meteorology*, 122(1–2), 95–109. https://doi.org/10.1016/j.agrformet.2003.09.003

Villa, T. F., Gonzalez, L. F., Miljevic, B., & Ristovski, Z. (2016). An Overview of Small Unmanned Aerial Vehicles for Air Quality Measurements: Present Applications and Future Prospectives. *Sensors*, July. https://doi.org/10.3390/s16071072

Wang, J. Y., Luo, B., Zeng, M., & Meng, Q. H. (2018). A wind estimation method with an unmanned rotorcraft for environmental monitoring tasks. *Sensors* (Switzerland), 18(12). https://doi.org/10.3390/s18124504

Wieser, A., Fiedler, F., & Corsmeier, U. (2001). The Influence of the Sensor Design on Wind Measurements With Sonic Anemometer Systems. *Journal of Applied Meteorology and Climatology*, 18, 1585–1608. https://doi.org/10.1175/1520-0426(2001)018<1585:TIOTSD>2.0.CO;2

Wilczak, J. M., Oncley, S. P., & Stage, S. A. (2001). Sonic anemometer tilt correction algorithms. *Boundary-Layer Meteorology*, 99(1), 127–150. https://doi.org/10.1023/a:1018966204465

Wyngaard, J. C. (1981). Cup, Propeller, Vane, and Sonic Anemometers in Turbulence research. *Annual Review Fluid Mechanics*, 399–423.

Wyngaard, J., & Zhang, S.-F. (1985). Transducer-Shadow Effects on Turbulence Spectra Measured by Sonic Anemometers. *In Journal of Atmospheric and Oceanic Technology* (pp. 548–558). https://doi.org/10.1175/1520-0426(1985)002<0548:TSEOTS>2.0.CO;2

Xing, Z. W., Zhang, Y. M., Su, C. Y., & Qu, Y. H. (2019). Measuring the Horizontal Wind for Forest Fire Monitoring Using Multiple UAVs. 2019 *Chinese Control Conference* (CCC).

Yamartino, R. J. (1984). A Comparison of Several “Single-Pass” Estimators of the Standard Deviation of Wind Direction. *Journal of Climate and Applied Meteorology*.

Yeo, D., Shrestha, E., Paley, D. A., & Atkins, E. M. (2015). An Empirical Model of Rotorcrafy UAV Downwash for Disturbance Localization and Avoidance. January, 1–15. https://doi.org/10.2514/6.2015-1685

Yoon, S., Lee, H. C., & Pulliam, T. H. (2016). Computational Analysis of Multi-Rotor Flows. 54th AIAA *Aerospace Sciences Meeting*, 1–11.

Zhang, H., Chen, J., & Park, S. (2000). Turbulence Structure in Unstable Conditions Over Various Surfaces. 5(1), 243–261.

Appendix A: TSM Angle of Attack and Transducer Shadowing Test Results

Yaw (ψ°)	Pitch (θ°)	Test	Low Speed			Medium Speed			High Speed		
			Pitot WS (ms^{-1})	TSM WS (ms^{-1})	TSM WD °	Pitot WS (ms^{-1})	TSM WS (ms^{-1})	TSM WD °	Pitot WS (ms^{-1})	TSM WS (ms^{-1})	TSM WD °
0	0	1	3.31	2.41	355.96	9.59	8.15	358.14	13.97	12.51	358.16
10	0	2	3.31	3.30	355.76	9.59	9.63	354.87	13.97	14.12	354.95
20	0	3	3.32	3.36	346.74	9.60	9.80	359.40	13.97	14.76	20.31
30	0	4	3.31	3.14	30.01	9.60	9.70	31.61	13.96	14.86	32.53
40	0	5	3.31	2.99	46.33	9.60	9.74	44.31	13.95	14.20	40.83
50	0	6	3.31	2.86	57.43	9.59	8.24	357.68	13.95	13.30	359.46
60	0	7	3.31	3.15	63.72	9.59	8.88	357.48	13.95	13.99	357.98
70	0	8	3.31	2.68	81.89	9.59	10.95	76.64	13.95	15.52	73.65
80	0	9	3.31	2.84	93.73	9.58	8.79	358.98	13.94	13.66	82.74
90	0	10	3.31	2.89	102.61	9.58	9.08	92.79	13.94	14.71	93.18

Yaw (ψ°)	Pitch (θ°)	Test	Low Speed			Medium Speed			High Speed		
			Pitot WS (ms^{-1})	TSM WS (ms^{-1})	TSM WD °	Pitot WS (ms^{-1})	TSM WS (ms^{-1})	TSM WD °	Pitot WS (ms^{-1})	TSM WS (ms^{-1})	TSM WD °
0	10	11	3.31	2.38	342.24	9.58	7.14	359.15	13.93	11.08	1.22
10	10	12	3.31	3.02	352.59	9.59	8.51	354.77	13.92	12.93	359.81
20	10	13	3.31	3.35	347.53	9.59	9.64	20.38	13.92	13.99	20.26
30	10	14	3.32	3.25	349.45	9.59	9.64	34.98	13.91	14.66	35.80
40	10	15	3.31	3.11	352.53	9.59	8.73	42.95	13.91	12.23	46.06
50	10	16	3.31	2.51	50.15	9.58	7.77	354.95	13.91	12.04	354.92
60	10	17	3.31	2.59	359.38	9.58	9.01	356.81	13.91	14.16	357.36
70	10	18	3.31	2.89	71.43	9.58	10.73	74.81	13.91	12.55	355.54
80	10	19	3.30	2.72	89.55	9.58	9.35	84.68	13.91	13.56	80.56
90	10	20	3.30	2.93	96.82	9.57	9.04	92.51	13.90	13.38	359.69
0	20	21	3.30	2.27	359.07	9.59	6.89	357.95	13.91	8.86	343.44
10	20	22	3.31	2.85	353.01	9.59	6.37	350.02	13.91	10.48	350.44
20	20	23	3.31	3.30	349.40	9.58	7.35	30.62	13.91	13.37	25.40
30	20	24	3.31	3.09	346.59	9.58	8.87	39.06	13.91	12.84	37.08
40	20	25	3.31	2.90	354.21	9.59	9.12	42.64	13.91	16.39	354.20
50	20	26	3.31	2.90	356.22	9.58	8.69	353.71	13.91	13.39	351.71
60	20	27	3.31	2.75	62.40	9.58	9.50	354.91	13.91	14.95	356.34
70	20	28	3.31	2.87	71.57	9.58	9.38	358.78	13.90	14.77	359.23
80	20	29	3.31	2.66	88.89	9.57	8.66	355.96	13.90	13.37	359.96
90	20	30	3.31	2.90	93.95	9.57	9.12	93.37	13.90	14.12	93.64
0	30	31	3.31	1.90	337.07	9.57	4.86	326.32	13.89	5.35	333.76
10	30	32	3.31	2.19	354.80	9.58	7.73	359.38	13.90	8.37	14.52
20	30	33	3.31	2.67	348.32	9.58	7.79	20.90	13.90	11.10	27.91
30	30	34	3.31	2.87	345.67	9.58	10.17	341.22	13.90	10.82	37.93
40	30	35	3.31	2.76	344.81	9.57	10.74	342.49	13.90	14.02	349.56
50	30	36	3.31	3.48	359.87	9.57	9.23	346.53	13.90	14.95	352.46
60	30	37	3.31	2.94	358.34	9.58	10.47	353.57	13.90	15.10	358.14
70	30	38	3.32	2.96	358.26	9.58	9.05	353.66	13.89	14.25	72.19
80	30	39	3.31	2.82	84.39	9.56	8.82	354.87	13.90	13.71	83.01
90	30	40	3.31	2.63	98.06	9.56	8.80	91.02	13.89	13.21	94.14

Yaw (ψ°)	Pitch (θ°)	Test	Low Speed			Medium Speed			High Speed		
			Pitot WS (ms^{-1})	TSM WS (ms^{-1})	TSM WD °	Pitot WS (ms^{-1})	TSM WS (ms^{-1})	TSM WD °	Pitot WS (ms^{-1})	TSM WS (ms^{-1})	TSM WD °
0	-10	41	3.31	2.80	352.69	9.58	9.72	358.32	13.96	14.71	356.42
10	-10	42	3.31	1.80	338.47	9.58	10.21	359.83	13.96	15.15	352.77
20	-10	43	3.31	2.79	20.66	9.58	9.87	358.13	13.95	14.56	355.09
30	-10	44	3.31	3.05	37.88	9.57	9.94	32.84	13.95	15.27	359.78
40	-10	45	3.31	3.41	53.14	9.57	9.56	359.63	13.95	14.53	358.37
50	-10	46	3.31	3.21	62.66	9.57	8.80	358.89	13.94	14.09	357.35
60	-10	47	3.31	3.01	65.58	9.57	9.15	356.96	13.94	14.50	357.86
70	-10	48	3.32	3.01	72.32	9.57	11.30	77.11	13.94	16.24	75.51
80	-10	49	3.32	2.65	89.19	9.56	8.76	80.05	13.94	13.72	84.41
90	-10	50	3.31	2.92	101.90	9.57	9.17	95.25	13.94	13.95	94.76
0	-20	51	3.30	2.57	343.00	9.57	10.26	359.72	13.94	14.81	357.67
10	-20	52	3.30	3.30	352.98	9.58	10.33	19.30	13.94	15.16	18.73
20	-20	53	3.30	3.28	353.17	9.57	9.27	28.94	13.94	13.70	37.98
30	-20	54	3.30	3.24	359.04	9.57	9.59	30.88	13.94	14.03	33.88
40	-20	55	3.30	3.10	45.18	9.57	9.99	354.88	13.93	14.89	41.71
50	-20	56	3.30	2.88	54.21	9.57	9.22	356.09	13.93	14.37	53.03
60	-20	57	3.30	3.02	65.85	9.57	9.26	356.07	13.94	14.32	60.47
70	-20	58	3.30	2.69	82.44	9.57	11.28	77.90	13.93	17.15	78.96
80	-20	59	3.30	2.83	94.64	9.56	8.65	81.47	13.94	17.16	98.96
90	-20	60	3.30	2.78	102.97	9.56	9.01	94.39	13.93	13.94	105.87
0	-30	61	3.31	2.73	358.71	9.58	10.16	1.23	13.94	14.01	0.69
10	-30	62	3.30	2.47	345.11	9.58	8.05	20.71	13.93	15.46	21.42
20	-30	63	3.30	2.86	348.78	9.57	9.13	35.31	13.93	11.73	41.66
30	-30	64	3.30	3.07	358.69	9.56	9.13	33.25	13.92	14.10	52.10
40	-30	65	3.31	3.29	46.81	9.56	10.18	351.67	13.92	13.43	48.07
50	-30	66	3.30	3.19	55.40	9.57	9.45	351.00	13.92	14.58	52.19
60	-30	67	3.31	2.95	65.96	9.56	9.83	358.32	13.93	14.29	63.23
70	-30	68	3.31	2.85	73.48	9.57	11.16	77.93	13.92	15.35	80.58
80	-30	69	3.31	2.63	93.07	9.56	8.61	81.13	13.93	17.54	98.72
90	-30	70	3.31	2.90	97.50	9.57	9.09	95.94	13.93	13.41	100.09